Cell Reports
Medicine

Article

ATM deficiency drives phenotypic diversity and Purkinje cell degeneration in a macaque model of ataxia-telangiectasia

Graphical abstract

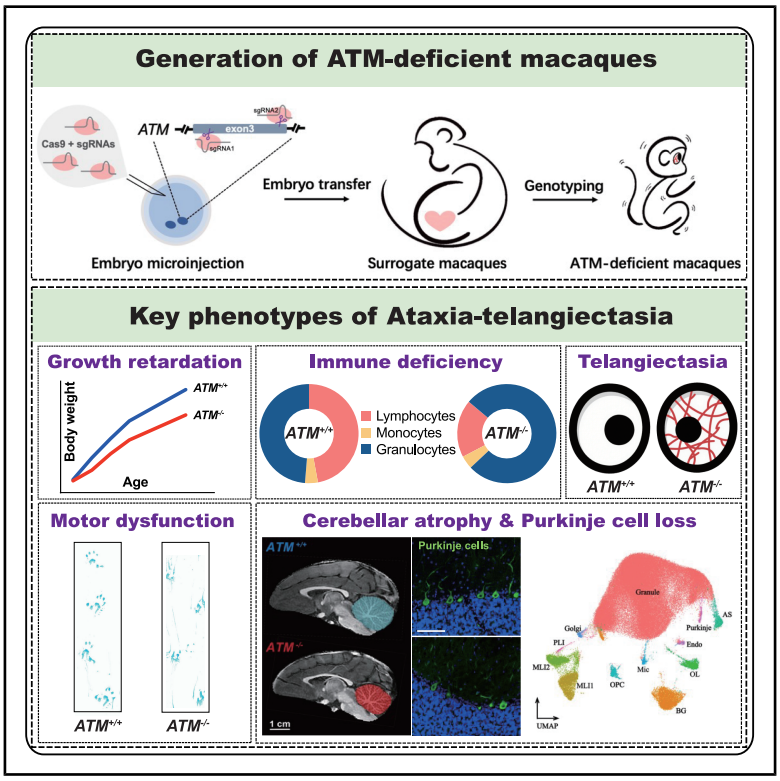

Authors

Kaiyu Xu, Ying Zhang, Yongxuan Chen, ..., Yong-Gang Yao, Dong-Dong Wu, Jiali Li

Correspondence

yaoyg@mail.kiz.ac.cn (Y.-G.Y.), wudongdong@mail.kiz.ac.cn (D.-D.W.), jiali.li@hmhn.org (J.L.)

In brief

Xu et al. report that CRISPR-Cas9-engineered ATM-deficient rhesus macaques model key features of ataxia-telangiectasia, including growth retardation, immune deficiency, and most critically, early-onset cerebellar atrophy. This model provides deeper insights into the pathogenesis of A-T and represents a promising and valuable platform for developing therapeutic strategies.

Highlights

- CRISPR-Cas9-generated ATM deficiency in macaque models human A-T
- ATM-deficient macaques faithfully recapitulate key phenotypes of human A-T
- Progressive cerebellar atrophy with early onset is observed in ATM-deficient macaques
- ATM deficiency causes Purkinje cell loss and transcriptomic shifts in cerebellar cell types

Xu et al., 2025, Cell Reports Medicine 6, 102355
September 16, 2025
https://doi.org/10.1016/j.xcrm.2025.102355

CellPress

Cell Reports Medicine

CellPress
OPEN ACCESS

Article

ATM deficiency drives phenotypic diversity and Purkinje cell degeneration in a macaque model of ataxia-telangiectasia

Kaiyu Xu,[1,7] Ying Zhang,[1,7] Yongxuan Chen,[1,2,7] Xiaojia Zhu,[1,2,7] Yu Li,[1,7] Longbao Lv,[1,2,7] Xiechao He,[1] Zhengfei Hu,[1] Yifan Li,[1] Maosen Ye,[1] Dewei Jiang,[1] Zhanlong He,[3] Weihua Jin,[3] Yanyan Li,[3] Xiaomei Yu,[1] Deng-Feng Zhang,[1] Karl Herrup,[4,8] Ping Zheng,[1,2,8] Yong-Gang Yao,[1,2,*] Dong-Dong Wu,[1,2,*] and Jiali Li[1,5,6,9,*]

[1]State Key Laboratory of Genetic Evolution and Animal Models, Key Laboratory of Animal Models and Human Disease Mechanisms of Yunnan Province, Yunnan Engineering Center on Brain Disease Models, KIZ-CUHK Joint Laboratory of Bioresources and Molecular Research in Common Diseases, National Research Facility for Phenotypic and Genetic Analysis of Model Animals (Primate Facility), National Resource Center for Non-Human Primates, Kunming Institute of Zoology, Chinese Academy of Sciences, Kunming, Yunnan, China
[2]Kunming College of Life Science, University of Chinese Academy of Sciences, Kunming, Yunnan, China
[3]Institute of Medical Biology, Chinese Academy of Medical Sciences, Peking Union Medical College, Kunming, Yunnan, China
[4]Department of Neurobiology, The University of Pittsburgh School of Medicine, Pittsburgh, PA, USA
[5]Department of Neurology, Hackensack Meridian School of Medicine, Nutley, NJ, USA
[6]Present address: JFK Neuroscience Institute, Hackensack Meridian Health JFK University Medical Center, Edison, NJ, USA
[7]These authors contributed equally
[8]Senior author
[9]Lead contact
*Correspondence: yaoyg@mail.kiz.ac.cn (Y.-G.Y.), wudongdong@mail.kiz.ac.cn (D.-D.W.), jiali.li@hmhn.org (J.L.)
https://doi.org/10.1016/j.xcrm.2025.102355

SUMMARY

Ataxia-telangiectasia (A-T) is a hereditary neurodegenerative disorder caused by mutations in the ATM (ataxia-telangiectasia mutated) gene. Although existing rodent models reproduce some of the multi-systemic features of A-T, they notably fail to recapitulate the severe neurological manifestations, particularly the profound cerebellar atrophy and associated ataxia. To address this limitation, we have generated ATM-deficient rhesus macaques using CRISPR-Cas9. These macaques exhibit hallmark features of A-T, including growth retardation, lymphopenia, elevated a-fetoprotein levels, oculocutaneous telangiectasias, heightened sensitivity to ionizing radiation, and most critically, cerebellar atrophy, Purkinje cell loss, and early-stage cerebellar neurodegeneration leading to significant motor impairments. Single-nucleus transcriptomic profiling of the cerebellum revealed pronounced gene expression changes associated with ATM deficiency, particularly in molecular layer interneurons (MLIs), which are implicated in Purkinje cell loss. This non-human primate model provides deeper insights into the pathogenesis of A-T and represents a promising and valuable platform for developing therapeutic strategies.

INTRODUCTION

Ataxia-telangiectasia (A-T) is a rare autosomal recessive disorder characterized by a spectrum of clinical features, including progressive cerebellar neurodegeneration (ataxia), oculocutaneous telangiectasias, immunodeficiency, growth retardation, incomplete sexual maturation, endocrine abnormalities, heightened sensitivity to radiation, and elevated cancer risk.[1–8] A-T is caused by mutations in the ataxia telangiectasia mutated (*ATM*) gene, located on the long arm of chromosome 11 (11q22.3) in humans.[9,10] Disease mutations are distributed throughout the entire *ATM* gene, without a discernible mutational hot spot.[11] What all mutations have in common is diminished ATM kinase activity.

ATM encodes a multifunctional protein kinase belonging to the phosphoinositide 3-kinase-related kinases family whose activities govern a cascade of crucial downstream protein pathways.[12,13] These include tumor suppressor proteins such as p53 and BRCA1, the checkpoint kinase CHK2, checkpoint proteins RAD17 and RAD9, and DNA repair protein NBS1.[4,9] Despite identifying numerous proteins as ATM substrates, the mechanism by which ATM deficiency triggers early-onset cerebellar degeneration remains unclear, perhaps because the loss of ATM function is associated with a wide range of cellular activities, including mitochondrial dysfunction, poly (ADP-ribose) polymerase (PARP) hyperactivation, deregulated epigenetics, disrupted calcium homeostasis, and protein aggregation.[14–20] As ATM plays a crucial role in DNA damage repair[21] and many other metabolic functions,[22,23] the result is a multisystemic disease that confines the patient to a wheelchair, shortens their life span and currently has no effective therapeutic intervention.[24–26]

Compounding the problem, the field currently lacks accurate models of A-T making it next to impossible to develop effective therapies.[4,27]

Developing physiologically relevant animal models remains a critical priority for studying this complex disorder. Notably, murine models expressing kinase-dead ATM variants display embryonic lethality, highlighting the challenges of recapitulating human pathology in rodent systems.[28] Since the cloning of the gene nearly three decades ago a number of rodent lines bearing *Atm* mutations have been created.[29–31] Many features of the A-T phenotype are captured by these models including immunodeficiency, heightened sensitivity to radiation, predisposition to cancer, infertility, and neurological abnormalities.[29] Yet none of the current ATM-deficient mouse models develop any significant cerebellar neurodegeneration, one of the most prevalent and debilitating features observed in A-T patients.[27–29] As with many human disease models species-specific differences between mouse and human make it difficult to generate a precise replicate of the human condition, particularly for disease that impact the nervous system.[32–34] The cerebellum, for example, has significantly expanded during primate evolution, leading to a greater diversity of cell types and molecular functions.[35–38] Although the cerebellum is highly conserved across mammals, studies of the developing human cerebellum have revealed differences in cellular composition and differentiation that differ measurably from those observed in mice.[39–41] The human cerebellum features an exceptionally intricate cytoarchitecture and an extensive connectivity network,[42,43] which may endow it with primate-specific functions.

The rhesus macaques (*Macaca mulatta*), like humans, undergoes altricial development, and born with open eyes and undergoing progressive acquisition of motor skills. Initial grasping and climbing behaviors appear at around one month, independent climbing by three months, and motor proficiency is typically achieved by six months.[44] Weaning generally occurs between six and twelve months, with females reaching sexual maturity by 3–4 years and initiating reproduction, while males attain competitive breeding capacity by 5–6 years[45,46] In managed care settings, rhesus macaques can live up to 30–35 years[47,48] These developmental and lifespan characteristics, along with close neuroanatomical and physiological homology to humans, make them particularly well-suited for modeling brain diseases.[33,49]

The application of CRISPR-Cas9 genome editing in non-human primates (NHPs) has enabled precise modeling of human genetic disorders.[33,49,50] For instance, dystrophin-edited macaques replicate features of muscular dystrophy,[51,52] *PSEN1*-mutated cynomolgus monkeys model Alzheimer's disease pathology,[53] *SHANK3*-edited macaques exhibit behavioral phenotypes reminiscent of autism and Phelan-McDermid syndrome,[32] *ANK2* depletion in primates results in severe brain volume loss,[34] and *PDX1*-mutant cynomolgus macaques exhibited pancreatic agenesis.[54]

Here, we aimed to establish an NHP model of A-T by generating ATM-deficient rhesus macaques using CRISPR-Cas9 gene editing. Firstly, we observed classical A-T phenotypes in the mutant animals, including growth retardation, lymphopenia, elevated alpha-fetoprotein (AFP), oculocutaneous telangiectasias, motor dysfunction, progressive cerebellar degeneration, and Purkinje cell loss. Subsequently, we applied single-nucleus transcriptomic profiling to reveal ATM deficiency-associated gene expression changes across diverse cerebellar cell types. Finally, we demonstrated that this NHP model offers critical insights into the molecular basis of A-T neuropathogenesis and provides a valuable platform for therapeutic development.

RESULTS

Generation of ATM-deficient rhesus macaques using CRISPR-Cas9-mediated gene targeting in one-cell embryos

The *ATM* gene in rhesus macaques, located on chromosome 14, encodes a protein composed of 3,056 amino acids, sharing an impressive 97.87% sequence identity with the human ATM protein. This high similarity contrasts with the 84.08% sequence identity between the ATM proteins of humans and mice (Figure S1A). To create ATM-deficient macaques, pairs of single-guide RNAs (sgRNAs) were designed to target the macaque *ATM* gene. Their effectiveness was initially validated by co-transfecting the sgRNAs with Cas9 into COS-7 cells, which are derived from African green monkey kidney cells. Among the sgRNAs, those targeting exon 3 of the *ATM* gene demonstrated the highest editing efficiency in these cultured cells, as confirmed by PCR-cloning and Sanger sequencing analyses (Figure 1A). These frameshift mutations caused premature translational stop and possibly a complete loss of the functional ATM.

Following these *in vitro* assessments, we proceeded to perform zygotic injections of Cas9 protein and the exon 3-targeting sgRNAs into one-cell stage embryos (Figure S1B). This approach demonstrated a high mutation efficiency of the *ATM* gene in macaque embryos (Figures S1C and S1D). Of the seven rhesus macaque embryos analyzed, six were confirmed to be homozygous knockouts (85.7%), underscoring the robust efficiency of the gene-editing technique employed (Figure S1E). In the subsequent steps to generate ATM-deficient macaques (Figure S1F), 122 oocytes were harvested and subjected to *in vitro* fertilization via introcytoplasmic sperm injection. Zygotes were microinjected, resulting in 88 viable zygotes. Of these, 55 developed normally and were subsequently transferred into 18 surrogate females (Figure S1G). This process led to three pregnancies, culminating in two healthy live births and one birth at 165 days gestation via caesarean section due to dystocia. The resulting macaques-two males (A1: no. 21365, A2: no. 21397) and one female (A3: no. 21408) were all successfully delivered and have since been carefully monitored (Figures 1B and 1C). Three wild-type neonatal macaques, matched by gender and age (within three days of birth), were selected as controls and designated as C1 (no. 21367, male), C2 (no. 21053, male), and C3 (no. 21410, female). Notably, while A2 and C2 required human rearing due to dystocia-related complications, the remaining macaques were reared by their receipt (for gene-edited infants) or biological mothers (for wild-type infants).

To confirm the success of the gene editing, ear punch tissues and peripheral blood samples were collected from the three gene-manipulated macaques. Analysis revealed the anticipated frameshift mutations in exon 3 of the *ATM* gene in all three

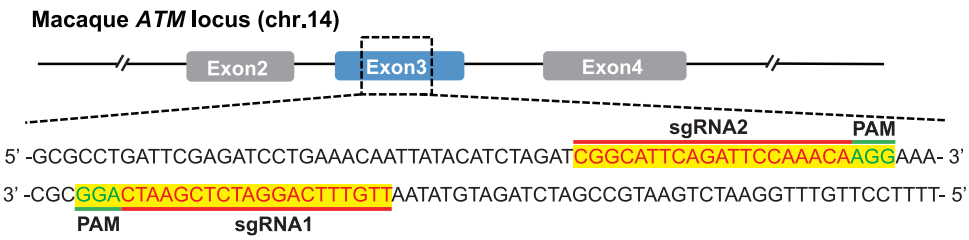

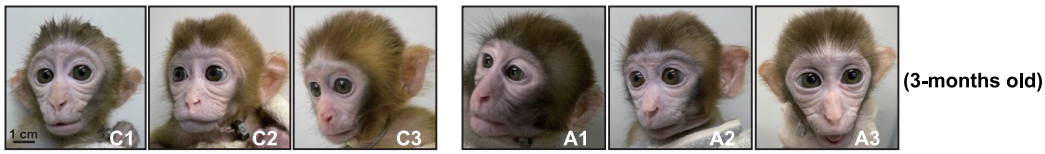

Animal code	Animal ID	Gender	Date of birth (d/m/y)	Gestation cycle (days)	Method of delivery	Genotype	Raising pattern
A1	21365	Male	30/6/2021	170	Eutocia	*ATM* $^{-/-}$	Breast feeding
A2	21397	Male	17/7/2021	165	C-section	*ATM* $^{-/-}$	Artificial feeding
A3	21408	Female	24/7/2021	172	Eutocia	*ATM* $^{-/-}$	Breast feeding
C1	21367	Male	30/6/2021	160	Eutocia	*ATM* $^{+/+}$	Breast feeding
C2	21053	Male	14/7/2021	150	Eutocia	*ATM* $^{+/+}$	Artificial feeding
C3	21410	Female	25/7/2021	160	Eutocia	*ATM* $^{+/+}$	Breast feeding

Figure 1. Generation of ATM-deficient macaques

(A) Schematic representation of the wild-type macaque *ATM* gene structure, highlighting the targeted exon 3 region. The magnified panels display the annotated sequences of the guide RNAs (gRNAs; red) and the protospacer adjacent motif (PAM; green) on both DNA strands within exon 3.

(B) Detailed information of all macaques (ATM-deficient macaques, A1, A2, and A3; wild-type control macaques, C1, C2, and C3) in this study.

(C) Photographs of all macaques at 3 months of age. The images include controls (C1, C2, and C3; $ATM^{+/+}$) and ATM-deficient (A1, A2, and A3; $ATM^{-/-}$) macaques. Scale bars, 1 cm.

(D) Partial sequence alignment of the *ATM* exon 3 genotyped from skin DNA. At least 20 T-A clones of PCR products were analyzed via DNA sequencing. The PAM sequences are underlined and highlighted in green; insertions are marked in blue. The sizes and ratios of deletions (indicated by “−”) and insertions (indicated by “+”) are shown in parentheses.

(E) PCR detection of sgRNA/Cas9-mediated cleavage at the *ATM* exon 3, amplified from skin genomic DNA of ATM-deficient (A1, A2, and A3) and control (C1, C2, and C3) macaques.

(F) Immunoblot analysis showing the absence of ATM protein in fibroblasts collected from all macaques. β-actin served as a loading control.

(G) Illustration of animal experiment workflow in all macaques.

subjects (Figures 1D and 1E). To assess potential off-target effects, we employed Cas-OFFinder, a highly sensitive off-target prediction tool.[55] Remarkably, none of the 2,005 predicted off-target sites for the *ATM*-targeting sgRNAs exhibited mutations in the Cas9-edited macaques, confirming the high specificity of our gene-editing approach. Finally, we assessed ATM protein levels by western blotting. As expected, ATM protein was detected in fibroblasts from wild-type control macaques (C1, C2, and C3) but was absent in fibroblasts from all three gene-edited macaques (A1, A2, and A3; Figure 1F).

All animal experiments were conducted in strict accordance with established ethical and welfare guidelines. At two years of age, individuals A1 and C1 were euthanized for pathological evaluation (Figure S1H) and single-nucleus RNA sequencing (snRNA-seq) analysis. The remaining pairs (A2/C2 and A3/C3) continued to receive routine care for long-term monitoring of lifespan, disease progression, and potential therapeutic interventions (Figure 1G).

ATM-deficient macaques exhibit phenotypes resembling A-T patients

Our initial assessments focused on early developmental metrics, such as body weight and head circumference. ATM-deficient macaques showed no statistically significant differences in these parameters when compared to their counterparts during early development (Figures 2A–2C). As the macaques aged, gender-specific weight differences became apparent—females generally weighed less than males—yet these differences remained statistically insignificant because of limited number of animals. All macaques were born with normal physical appearance; however, by approximately six months of age, ATM-deficient individuals began to exhibit prominent telangiectasias, particularly dilated blood vessels in the eyes (Figure 2D), which is a phenotype not observed in Atm-mutant mice.[29] Subsequent serum analysis revealed a significant elevation in AFP levels in ATM-deficient macaques compared to controls (Figure 2E), with differences becoming apparent after 12 months of age. This is a notable finding, as elevated AFP is a characteristic biochemical marker frequently observed in patients with A-T.[9,56]

Additionally, we identified hyperactivation of PARP in fibroblasts derived from ATM-deficient macaques compared to those of controls (Figures 2F and 2G). PARP hyperactivation has been shown to be associated with cerebellar ataxia resulting from DNA damage.[57] To further assess the impact of ATM deficiency on cellular response to DNA damage, we subjected primary fibroblasts from both ATM-deficient macaques and controls to apoptosis and survival assays following exposure to ionizing radiation and the DNA-damaging agent etoposide (Figures S2A–S2D). As expected, ATM-deficient fibroblasts exhibited heightened sensitivity to both forms of DNA damage, resulting in increased apoptosis and reduced cell survival compared to controls (Figures 2H and S2B–S2D).

ATM deficiency leads to significant immune system impairments

Immune system dysfunction is a hallmark of A-T, a condition caused by mutations in the *ATM* gene.[58–60] To investigate the effects of ATM deficiency on the immune system, we conducted routine peripheral blood tests on ATM-deficient macaques every three months from birth. Most hematological indices, including those related to red blood cells, hemoglobin, and platelets, remained within normal ranges (Figures S3A–S3C). However, ATM-deficient macaques exhibited a significant reduction in leukocyte counts, with lymphocytes being particularly affected. White blood cell counts were markedly decreased in the ATM-deficient group at 12 and 15 months of age (Figure 3A). Lymphocyte counts were significantly lower than controls at 6, 15, and 21 months (Figure 3B), and the proportion of lymphocytes was also significantly reduced at 3, 6, and 18 months (Figure 3C). A comparative analysis of lymphoid tissues between an ATM-deficient macaque (A1, $ATM^{-/-}$) and a control (C1, $ATM^{+/+}$) at an age of 24 months revealed a marked reduction in the size of lymphoid organs, notably in the lymph nodes, spleen, and thymus (Figures 3D and S3D). Histological examinations further indicated significant atrophy and disrupted germinal center structures in axillary lymph node of ATM-deficient macaque A1 compared to control C1. Immunohistochemical staining highlighted a severe depletion of CD3-positive T cells and CD20-positive B cells in the lymphoid tissues of A1 compared to C1 (Figures S3E and S3F). Notably, the reduction in lymphocyte counts is clinically relevant, as lymphopenia is associated with an increased risk of cancer and infection in patients with A-T.[60]

In addition to these lymphoid abnormalities, a detailed histological analysis of liver, kidney, and muscle tissues from both $ATM^{-/-}$ (A1) and $ATM^{+/+}$ (C1) showed no apparent differences in tissue architecture (Figure S3G). Further examination revealed significant abnormalities in the lung tissue of an $ATM^{-/-}$ macaque, including widespread vascular expansion and notable inflammatory cell infiltration (Figure 3E). Interestingly, despite the severe lymphoid and pulmonary abnormalities, ATM deficiency did not result in decreased levels of immunoglobulins (IgA and IgG) in peripheral blood (Figures 3G and S3H). In contrast, IgM levels were notably elevated in ATM-deficient macaques (Figure 3F), which serve as a crucial indicator of poor prognosis in A-T patients.[58,61] The observed variations in lymphocyte maturation and immune homeostasis in ATM-deficient macaques underscore the complex role of ATM in immune function and offer critical insights into the pathophysiology of A-T.

Cerebellum-related neurobehavioral deficits in ATM-deficient macaques

Progressive impairment in the coordination of voluntary movement is a hallmark feature of A-T in patients.[62,63] To explore whether ATM deficiency leads to similar neurobehavioral deficits in macaques, we conducted a comprehensive series of tests designed to assess brain function associated with ATM deficiency (Figures S4A). Initially, we monitored the spontaneous locomotor activity of ATM-deficient macaques by recording daily home-cage videos. Quantitative analysis revealed that ATM-deficient macaques exhibited a marked reduction in exploratory behavior, preferring to remain on the ground rather than actively moving around their cages (Figures 4A and 4B). This behavior contrasted with the more active and inquisitive nature observed in control macaques.

To further investigate motor coordination, we employed the Kinema Tracer 3D gait analysis system (Kissei, Japan)[64] to

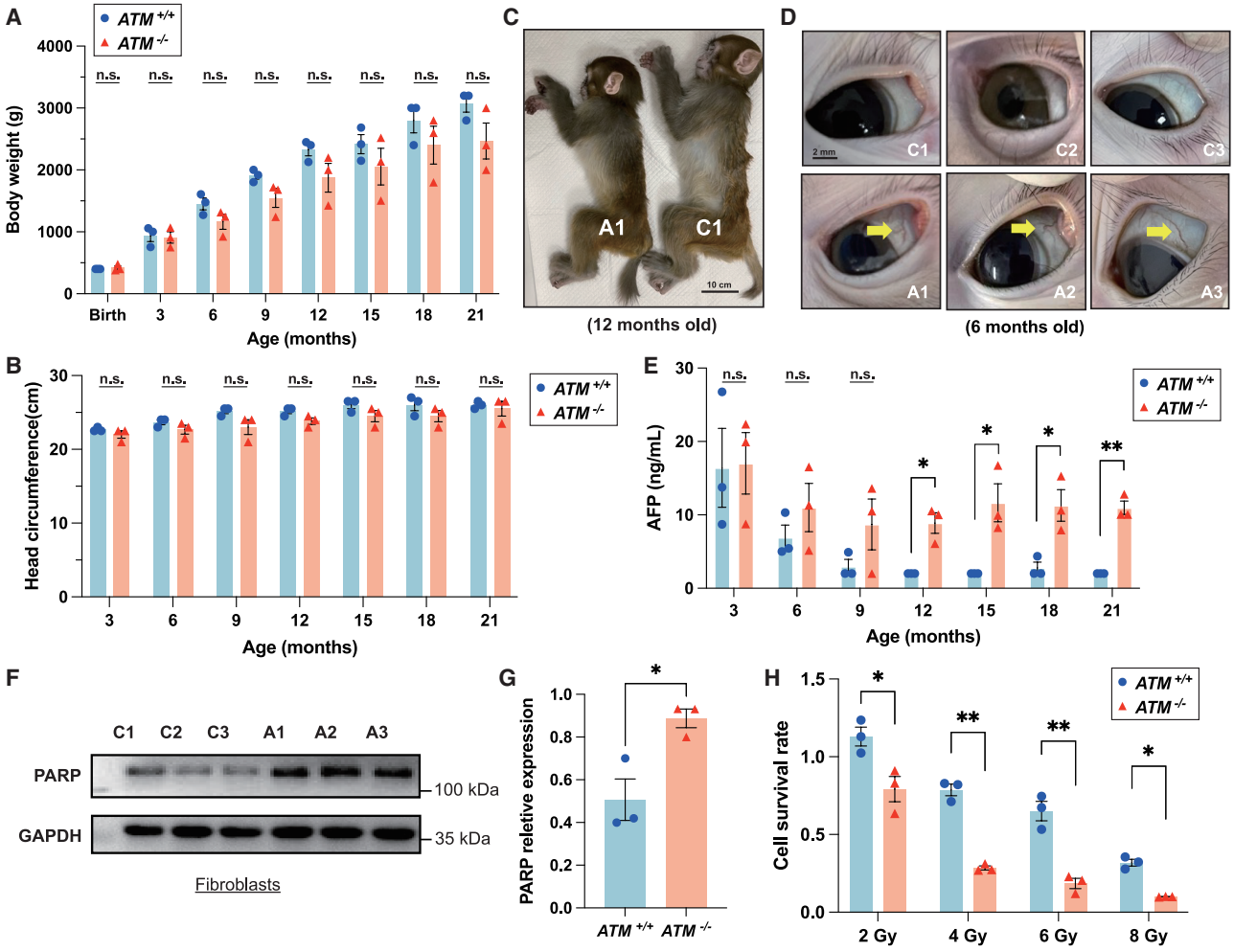

Figure 2. ATM-deficiency in macaques recapitulates canonical A-T phenotypes in humans

(A and B) Body weight (A) and head circumference (B) of control ($ATM^{+/+}$) and ATM-deficient ($ATM^{-/-}$) macaques after birth. Data are presented as mean ± SEM, with n = 3 macaques per group; n.s., no significance; unpaired t test.

(C) Representative photographs of control (C1; $ATM^{+/+}$) and ATM-deficient (A1; $ATM^{-/-}$) macaques at 12 months of age. Scale bars, 10 cm.

(D) Ocular telangiectasia observed in ATM-deficient macaques (A1, A2, and A3) but not in controls (C1, C2, and C3). Yellow arrows indicate the presence of telangiectasia. Scale bars, 2 mm.

(E) Serum levels of alpha-fetoprotein (AFP) in control and ATM-deficient macaques. Data are presented as mean ± SEM, with n = 3 macaques per group. *$p < 0.05$ and **$p < 0.01$; n.s., no significance; unpaired t test.

(F and G) Western blot analysis showing the expression of PARP in fibroblasts from ATM-deficient macaques and controls (F) and quantification (G). GAPDH was used as a loading control.

(H) The survival rate of fibroblasts from ATM-deficient macaques and controls after irradiation at different doses.

Data in (G and H) are presented as mean ± SEM, with n = 3 macaques per group. *$p < 0.05$ and **$p < 0.01$; unpaired t test.

evaluate macaque hindlimb function at an age of 15 months, which is approximately equivalent to 5 years of age in humans. The macaques were trained to walk bipedally on a treadmill, allowing for detailed footprint analysis to assess differences in ambulation between ATM-deficient and control macaques. The ATM-deficient macaques displayed a disordered and inconsistent stepping pattern (Figures 4C and 4D). Specifically, the ATM-deficient macaques exhibited significantly faster cadences, and larger stride widths, but shorter gait cycles and stride lengths compared to controls (Figures 4E–4H, and Videos S1, S2, S3, S4, S5, and S6). These findings suggest an abnormal gait pattern, indicative of ataxia. In addition to gait analysis, we evaluated manual dexterity using the Klüver board and vertical slit tasks, which assess the ability to manipulate objects to retrieve food pellets.[65,66] No statistically significant differences in manual dexterity were observed between ATM-deficient macaques and controls (Figures 4I, 4J, S4B, and S4C).

To evaluate cognitive functions related to the cerebrum, particularly learning and memory, we used the delayed-response task, a well-established test linked to prefrontal cortex activity.[67–69] This task was conducted in an improved Wisconsin General Test Apparatus (WGTA) adapted for juvenile macaques

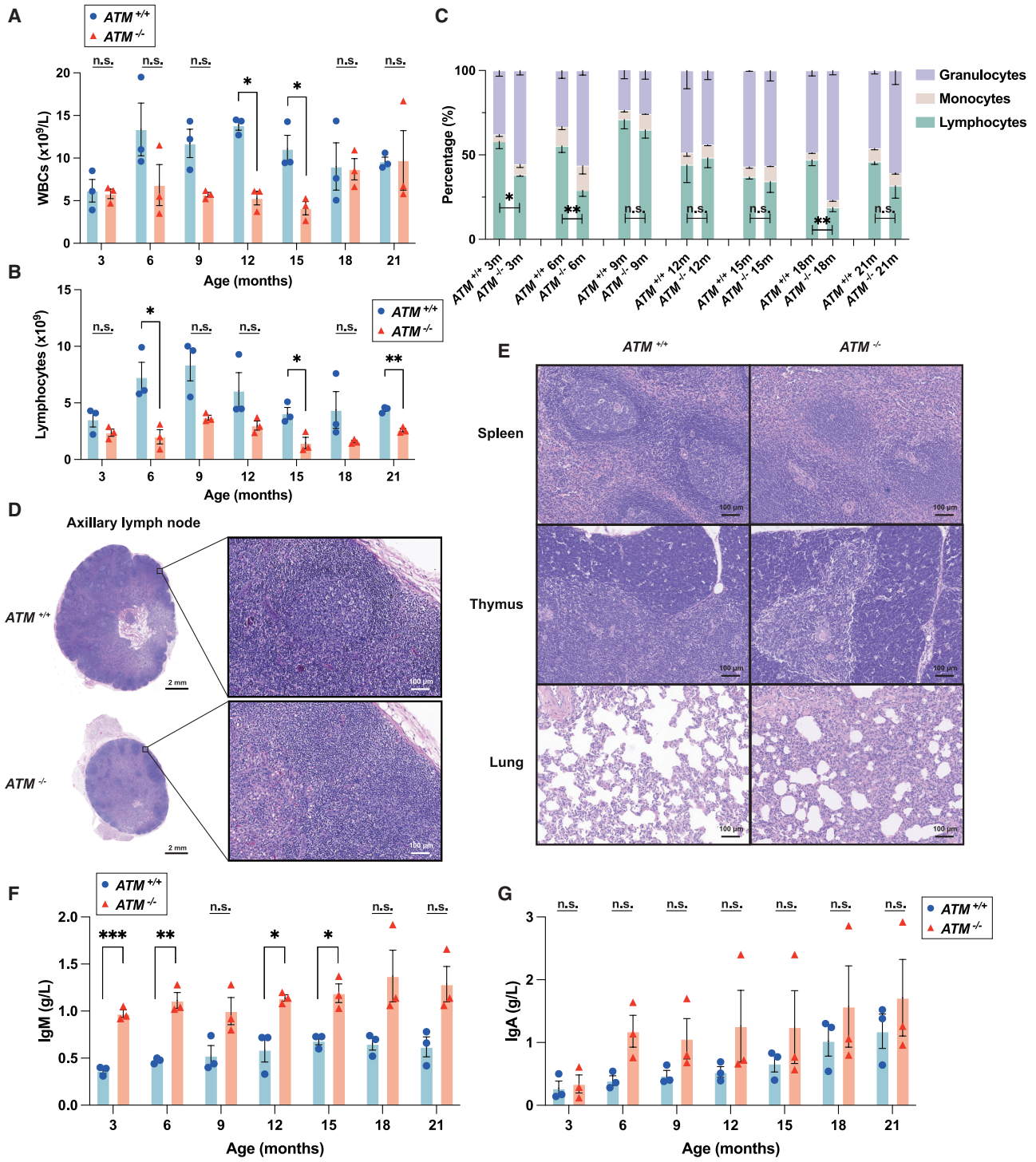

Figure 3. ATM deficiency in macaques results in reduced immune function

(A–C) Peripheral blood analyses of ATM-deficient and control macaques. ATM-deficient macaques exhibited significantly lower counts of white blood cells (A) and lymphocytes (B) during development compared to controls. The lymphocyte ratio (C) was also reduced in ATM-deficient macaques. Data are presented as mean ± SEM, with $n = 3$ macaques per group. $^{*}p < 0.05$ and $^{**}p < 0.01$; n.s., no significance; unpaired t test.

(D and E) Representative hematoxylin and eosin (H&E) stained sections showing tissue architecture in an ATM-deficient macaques (A1, $ATM^{-/-}$) compared to a control (C1, $ATM^{-/-}$). The axillary lymph node (D), spleen, thymus, and lung (E) tissues were examined. Scale bars: black panel, 2 mm; white panel, 100 μm.

(legend continued on next page)

(Figure 4K). No significant differences were observed between the ATM-deficient and control macaques in this task (Figures 4K and S4D–S4I). Therefore, a careful assessment of whether late-stage ATM deficiency affects upper limb dexterity and cognitive functions of macaques will be valuable for future research.

Brain MRI tracking reveals progressive cerebellar atrophy and altered cerebellum connectivity in ATM-deficient macaques

Neurodegeneration, particularly early-onset cerebellar atrophy, is one of the most debilitating aspects of A-T in patients.[70] To dynamically monitor aberrant growth in ATM-deficient macaques, we conducted regular non-invasive MRI scans every three months, starting at three months of age. Our analysis began by measuring the cerebellum and total brain volume of each macaque at various ages (Figure 5A). The ATM-deficient macaques consistently exhibited a significantly smaller cerebellar volume (Figure 5B) and reduced external cerebellar surface area (Figures S5A and S5B) compared to controls at each time point. Although the volume of other brain regions, excluding the cerebellum, was slightly reduced in ATM-deficient macaques, these differences were not statistically significant (Figure S5C). The control group exhibited sustained positive cerebellar volume growth trajectories throughout the observation period, as reflected by consistently positive volumetric change rates (Figure 5C). In stark contrast, the ATM-deficient group showed a progressive decline in cerebellar growth, culminating in a pathological shift to negative growth rate by 15 months of age (Figure 5C). This reversal in growth dynamics indicates a critical transition, wherein cerebellar atrophy begins to outweigh normal developmental expansion.

As the macaques aged, cerebellar atrophy in ATM-deficient individuals became increasingly pronounced. This atrophy was most rapid during the first 12 months of life, after which it continued at a slower pace, reaching its peak severity by 21 months (Figure 5D). These findings closely mirror the progressive cerebellar degeneration observed in human A-T patients. To gain a more detailed understanding of cerebellar atrophy, we divided the cerebellum into 17 subregions based on the Paxinos atlas.[71] Our analysis revealed that each cerebellar subregion in ATM-deficient macaques exhibited varying degrees of atrophy over time. Notably, the paraflocculus (PFL), Crus II, and Par regions within the cerebellar hemispheres displayed the most significant atrophy, with damage progressively extending from the hemispheres to the vermis (Figure 5D, bottom right). The most pronounced volume reductions were observed in the Par, PFL, Crus II, and the V-region of the motor cortex, suggesting that these areas may be particularly susceptible to damage.

Brain function is closely linked with the brain's geometry, such as its shape (contour and curvature).[72] To further quantify the geometric differences in the cerebellum, we utilized eigenvalue decomposition methods to analyze the cerebellar structure of each subject.[72] We found that the second through fourth eigenmodes (eigenmode 2–4) showed significantly larger eigenvalue ranges in ATM-deficient macaques compared to controls, indicating greater morphological differences (Figure S5D). For example, in geometric eigenmode 2, the cerebellum of ATM-deficient macaques appeared elongated along the proximal left-right axis, while in eigenmode 3, it was extended from the medial-ventral to external-dorsal direction, resulting in a flatter overall structure. These structural alterations gave the cerebellum of ATM-deficient macaques a "dried-out" appearance, in contrast to the fuller, more robust cerebellum observed in controls.

Altered functional connectivity has recently been recognized as a key biomarker of neuropathological states in a range of neurological and psychiatric disorders.[32] We collected resting-state fMRI data from both ATM-deficient and control macaques at 18 and 21 months of age, the stages at which morphological differences were most pronounced. Analysis of the mean functional connectivity within the cerebellar cortex and between the cerebellar cortex and cerebral cortex (intra-cerebellar and cerebello-to-cerebral connectivity) revealed a marked decrease in ATM-deficient macaques (Figures 5E and S5E). Specifically, intra-cerebellar connectivity decreased from an average strength of 0.2593 to 0.1945, while cerebello-to-cerebral connectivity dropped from 0.2107 to 0.1278. The most significant reductions in intra-cerebellar connectivity were observed in motor regions IV–VI and cognitive regions such as VIII, Par, Sim, and Crus I. Similarly, cerebello-to-cerebral connectivity was most severely impaired in areas VII–VIII, Par, Crus I, and Crus II (Figure S5E). Taken together, cerebellar fMRI data suggest that ATM-deficient macaques exhibit reduced resting-state connectivity, both locally and globally.

ATM deficiency induces vulnerability and degenerative changes in macaque cerebellar Purkinje cells

To identify neuropathological differences, we performed detailed histological analyses at both the light and ultrastructural levels. Gross histological examination revealed a reduction in cerebellar volume and abnormal morphology in the ATM-deficient macaque (A1) compared to the control (C1) (Figure 6A), while no significant differences were observed in the cerebral cortex or hippocampus between the two groups (Figures S6A–S6D). Immunohistochemical staining for DARPP32, a marker of Purkinje cells,[73,74] showed a marked decrease in the number of Purkinje cells in the ATM-deficient cerebellum, with fewer DARPP32-positive cells compared to the healthy control (Figures 6A–6C). Staining for aldolase C (AldoC), another established marker of Purkinje cells,[75] further confirmed a significant reduction in Purkinje cell density in the ATM-deficient group compared to controls (Figure S6E). Interestingly, we also observed a significant increase in microglial density with pronounced clustering within the white matter of the

(F and G) Elevated serum immunoglobulin IgM (F) and IgA (G) levels in ATM-deficient macaques compared to controls. Data are presented as mean ± SEM, with $n = 3$ macaques per group. $^{*}p < 0.05$, $^{**}p < 0.01$, and $^{***}p < 0.001$; n.s., no significance; unpaired t test. The ATM-deficient macaques had a generally higher level of serum immunoglobulin than those of control macaques, but the comparisons of levels at certain time points between the two groups showing no statistical difference, partially due to the small sample size.

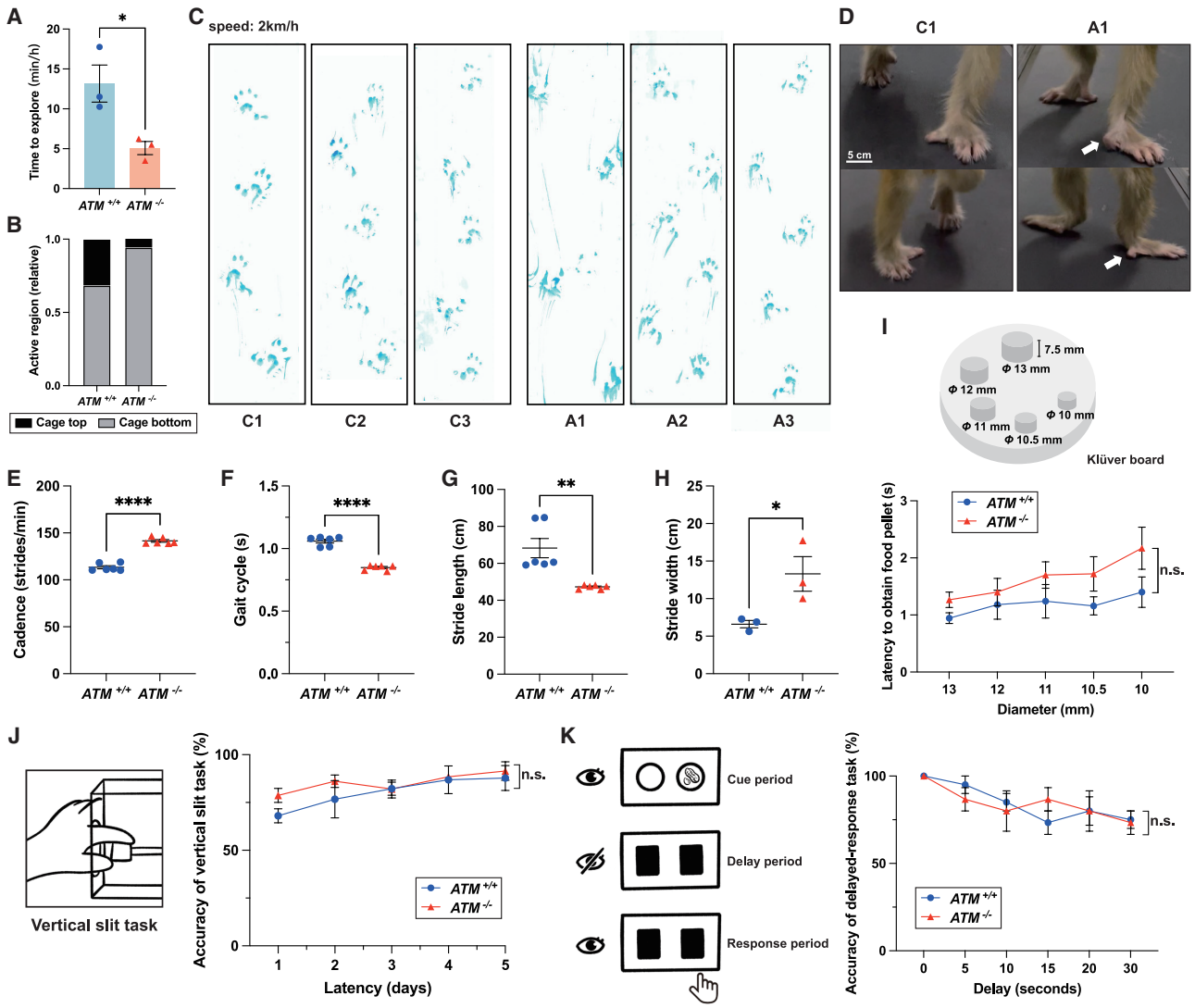

Figure 4. Behavioral abnormalities indicative of cerebellar dysfunction in ATM-deficient macaques

(A) ATM-deficient macaques exhibited reduced activity in their home cages at 3 months of age. Data are presented as mean ± SEM, with $n = 3$ macaques per group. $^{*}p < 0.05$; unpaired t test.

(B) ATM-deficient macaques primarily moved within the lower regions of the cage, indicating the limited range of motion.

(C) Representative footprint patterns from three controls (C1, C2, and C3; $ATM^{+/+}$) and three ATM-deficient macaques (A1, A2, and A3; $ATM^{-/-}$). The treadmill speed was set to 2 km/h.

(D) Photographs illustrating the bipedal gait of a control macaque (C1; $ATM^{+/+}$) compared to an ATM-deficient macaque (A1; $ATM^{-/-}$) at 15 months of age. Arrows highlight the inward buckling of the hallux in A1. Scale bars, 5 cm.

(E–H) Significant behavioral abnormalities in ATM-deficient macaques, including increased cadence (E), shortened gait cycle (F), reduced stride length (G), and increased stride width (H), compared to controls. Data are presented as mean ± SEM, with $n = 3$ macaques per group. $^{*}p < 0.05$, $^{**}p < 0.01$, and $^{****}p < 0.0001$; unpaired t test.

(I and J) Fine motor abilities of the upper limbs in ATM-deficient macaques were not significantly impaired, as assessed by the Klüver board (I) and vertical slit (J) tasks at 15 months of age.

(I) Schematic of the Klüver board (*top*) and testing results for ATM-deficient macaques and controls across bore diameters (10, 10.5, 11, 12, and 13 mm) (*botttom*).

(J) Schematic of the vertical slit task (window size: 30 × 6 mm) (*left*) and testing results, with the *x* axis representing the number of learning days and the *y* axis representing accuracy (*right*). Data are presented as mean ± SEM, with $n = 3$ macaques per group; n.s., no significance; unpaired t test.

(K) Learning and memory were not impaired in ATM-deficient macaques relative to controls. The delayed-response task in a modified Wisconsin General Test Apparatus (WGTA) suitable for young macaques (*left*) was used to perform the delayed-response trials (*right*). No significant differences were observed between controls and ATM-deficient macaques at various delay times (0, 5, 10, 15, 20, and 30 s). Data are presented as mean ± SEM, with $n = 3$ macaques per group; n.s., no significance; unpaired t test.

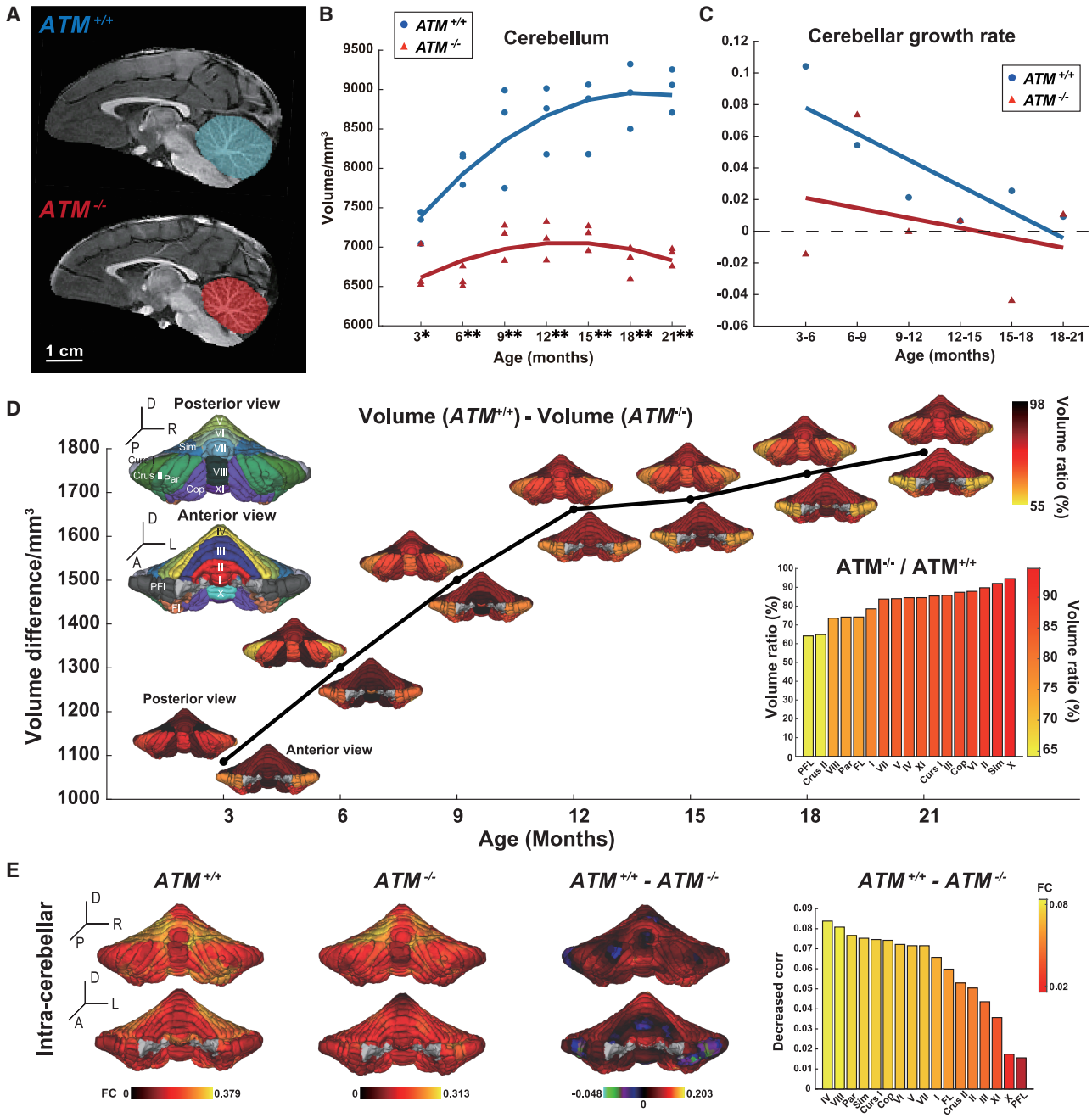

Figure 5. MRI scans reveal progressive cerebellar atrophy and degeneration in ATM-deficient macaques

(A) T1-weighted structural images of the brain at 21 months of age from a control macaque (C2; *top*) and an ATM-deficient macaque (A2; *bottom*).

(B and C) Volume (B) and growth rate analysis of the cerebellum (C) in control macaques ($ATM^{+/+}$, *blue*) and ATM-deficient macaques ($ATM^{-/-}$, *red*) at various time points. $n = 3$ macaques per group; $^{*}p < 0.05$ and $^{**}p < 0.01$; n.s., no significance; unpaired t test.

(D) Temporal differences in cerebellar volume between ATM-deficient and control macaques. The 3D maps above and below the dot plots illustrate the degree of atrophy across different cerebellar compartments (expressed as the percentage difference in volume relative to controls). Bars represent the average volume reduction in specific subregions over time. The schematic diagram provides the spatial distribution of cerebellar subregions from anterior and posterior views. Labels: A (anterior), P (posterior), R (right), L (left), and D (dorsal).

(E) Average functional connectivity (FC) within the cerebellum, comparing ATM-deficient macaques to controls. The graph on the right shows differences in intracerebellar functional connectivity between the two groups.

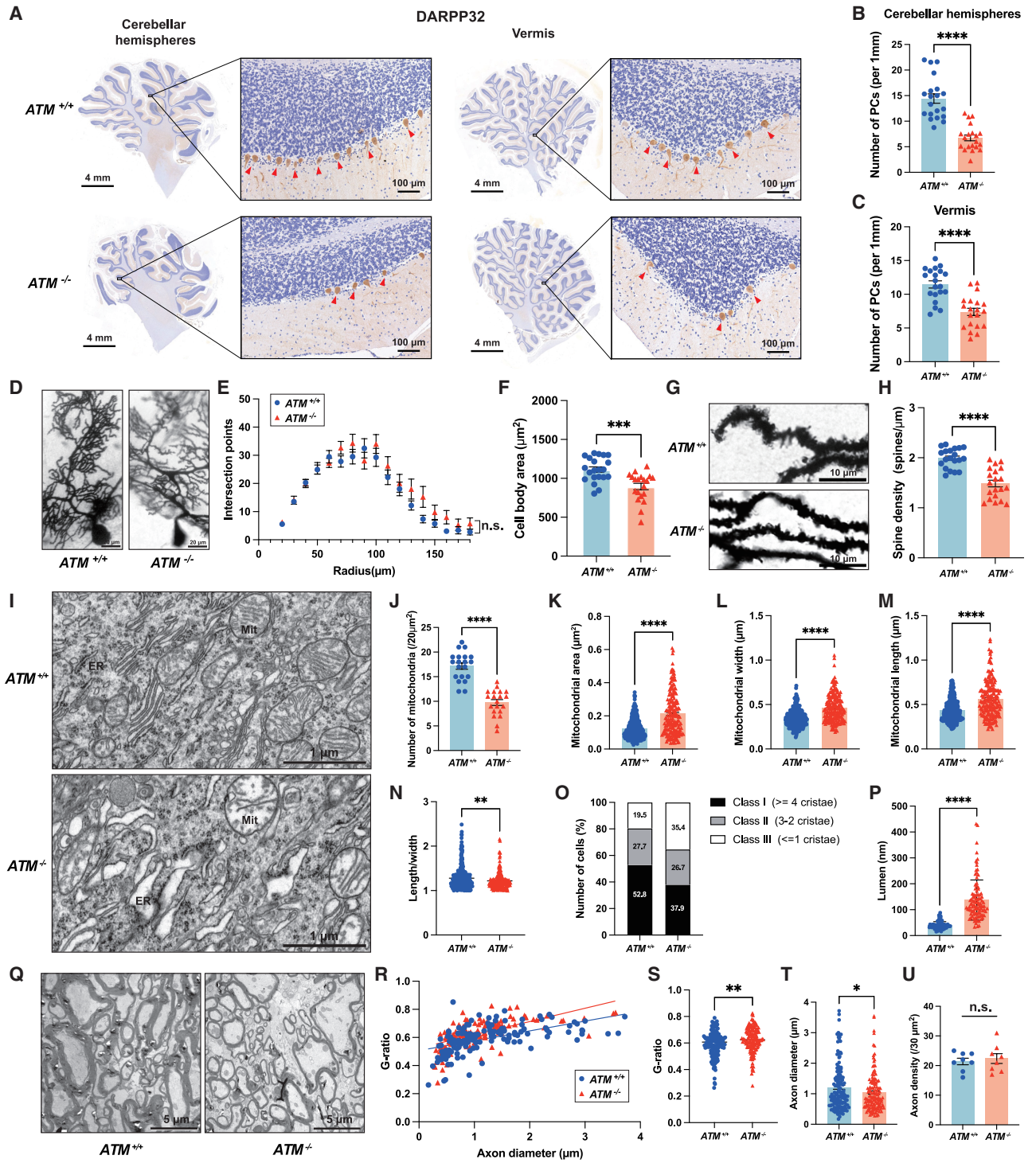

Figure 6. ATM deficiency leads to Purkinje cell vulnerability and degenerative changes

(A) Immunohistochemical staining for DARPP32, a marker for Purkinje cells, in cerebellar hemispheres and vermis sections from a control (C1; *ATM*$^{+/+}$) and an ATM-deficient (A1; *ATM*$^{-/-}$) macaque. Red arrows indicate DARPP32-positive Purkinje cells. Scale bars, 4.0 mm (*left*) and 100 µm (*right*) in hemispheres or vermis.

(B and C) A significant reduction of the number of DARPP32-positive Purkinje cells (PCs) in cerebellar hemispheres (B) and vermis (C) in ATM-deficient macaque (A1) compared to control (C1). Data are presented as mean ± SEM, with counts from at least two sections and ten visual fields per section. ****$p < 0.0001$; unpaired t test.

(legend continued on next page)

ATM-deficient cerebellum, while astrocyte numbers remained comparable to controls (Figures S6E and S6F). Further analysis using Golgi staining revealed no significant differences in the branching structure of Purkinje cells between ATM-deficient and control macaques. However, there was a notable decrease in cell body area and spine density in Purkinje cells from ATM-deficient macaques (Figures 6D–6H).

Given the critical role of mitochondria in cellular metabolism, particularly in high-energy-demanding cells such as neurons, we examined the impact of ATM deficiency on mitochondrial integrity. Previous studies have reported impaired mitochondrial function in ATM-deficient cultured cells.[9,76] In our study, transmission electron microscopy (TEM) analysis revealed significantly reduced numbers and morphologically aberrant mitochondria in Purkinje cells from ATM-deficient cerebellum (Figures 6I–6O). Additionally, we observed dilatation in the endoplasmic reticulum, Golgi complex, and nuclear membrane in ATM-deficient neurons (Figures 6I and 6P). These alterations indicate that ATM deficiency disrupts multiple cellular organelles, potentially contributing to neuronal dysfunction and degeneration.

To further explore the impact of ATM deficiency on cerebellar function, we assessed the state of cerebellar white matter. We measured the g-ratio, axon diameter, and myelin thickness-key metrics for evaluating axonal myelination.[77] Our findings revealed that the cerebellum of ATM-deficient macaques exhibited significantly thinner myelin sheaths, as indicated by an increased g-ratio, along with smaller axon diameters compared to controls (Figures 6Q–6U). These changes may be linked to the activation of microglia in the ATM-deficient white matter (Figures S6E and S6F). Despite these alterations, axon density remained unchanged, suggesting that while myelination is impaired, the overall number of axons is not significantly affected at the early stage of A-T.

Moreover, *in vivo* analysis using the TUNEL (terminal deoxynucleotidyl transferase dUTP nick end labeling) assay revealed striking differences in cerebellar apoptosis between ATM-deficient and control macaques. Specifically, the cerebellum of the ATM-deficient macaque (A1) exhibited a markedly higher incidence of apoptotic cells compared to age-matched controls (Figure S6G). Quantitative analysis showed a 3.7-fold increase in TUNEL-positive cells in the cerebellar cortex of A1 ($p < 0.001$, $n > 4$ fields per animal). This elevated apoptosis was particularly pronounced in the Purkinje cell layer and the internal granule cell layer, key regions affected in A-T. Furthermore, immunohistochemical analysis of cleaved caspase-3, a crucial executioner of apoptosis, corroborated the TUNEL results. Cerebellar sections from ATM-deficient macaques showed a 4.7-fold increase in cleaved caspase-3-positive cells compared to controls ($p < 0.001$, $n > 4$ fields per animal) (Figure S6H), indicating a heightened level of apoptosis likely associated with impaired DNA repair in the ATM-deficient cerebellum.

Single-nucleus transcriptome profiling of cerebellum in ATM-deficient macaque

To gain a deeper understanding of the molecular and cellular mechanisms underlying cerebellar dysfunction in ATM-deficient macaques, we conducted a comprehensive snRNA-seq analysis across various cerebellar regions, including the superior vermis (SV), anterior lobe (AL), posterior lobe (PL), and flocculus (FL) (Figure 7A). For this comparative analysis, samples were collected from a 24-month-old ATM-deficient macaque (A1), alongside an age- and sex-matched wild-type control (C1). Following rigorous quality control procedures (Figures S7A and S7B), we obtained a high-quality dataset comprising 121,791 cells suitable for downstream single-nucleus transcriptomic analysis. The dataset exhibited robust depth and coverage, with a median of 1,226 unique molecular identifiers (UMIs) per cell and a median of 744 genes expressed per cell. The final dataset consisted of 62,421 cells from the wild-type macaque (C1)

(D–H) Examination of Purkinje cell structure and dendritic spines in control and ATM-deficient macaque (A1) by Golgi staining.
(D) Representative images of Purkinje cells. Scale bars, 20 μm.
(E) Sholl analysis depicting the number of intersections of Purkinje cell branches and branchlets with concentric spheres centered on the cell soma.
(F) Quantification of Purkinje cell body area.
(G) Representative images showing dendritic spines of Purkinje cells. Scale bars, 10 μm.
(H) Quantification of dendritic spine density. Data are presented as mean ± SEM from at least five sections, with counts from five different Purkinje cells per section; n.s., no significance; unpaired t test.
(I–P) Ultrastructural abnormalities in Purkinje cells due to ATM deficiency.
(I) Representative electron microscopy images showing Purkinje cell ultrastructure in the cerebellar vermis. Mit, mitochondria; ER, endoplasmic reticulum. Scale bars, 10 μm.
(J) Number of mitochondria in Purkinje cells.
(K) Mitochondrial area.
(L) Mitochondrial width.
(M) Mitochondrial length.
(N) Mitochondrial aspect ratio.
(O) Percentage of different mitochondrial categories. Data include n = 195–343 mitochondria per group.
(P) Endoplasmic reticulum lumen width. Data include n = 20 ER sections per group. All data are presented as mean ± SEM from at least two sections, with counts from twenty different visual fields. $^{**}p < 0.01$ and $^{****}p < 0.0001$; unpaired t test.
(Q–U) Cerebellar myelin degeneration in ATM-deficient macaque (A1).
(Q) Ultrastructural images of myelin in the cerebellar vermis. Scale bars, 5 μm.
(R) Scatterplots of G-ratio indicating myelin thinning.
(S) Calculation of G-ratio showing decreased myelin thickness.
(T) Axon diameter measurements.
(U) Axon density analysis. $^{*}p < 0.05$ and $^{**}p < 0.01$; unpaired t test.

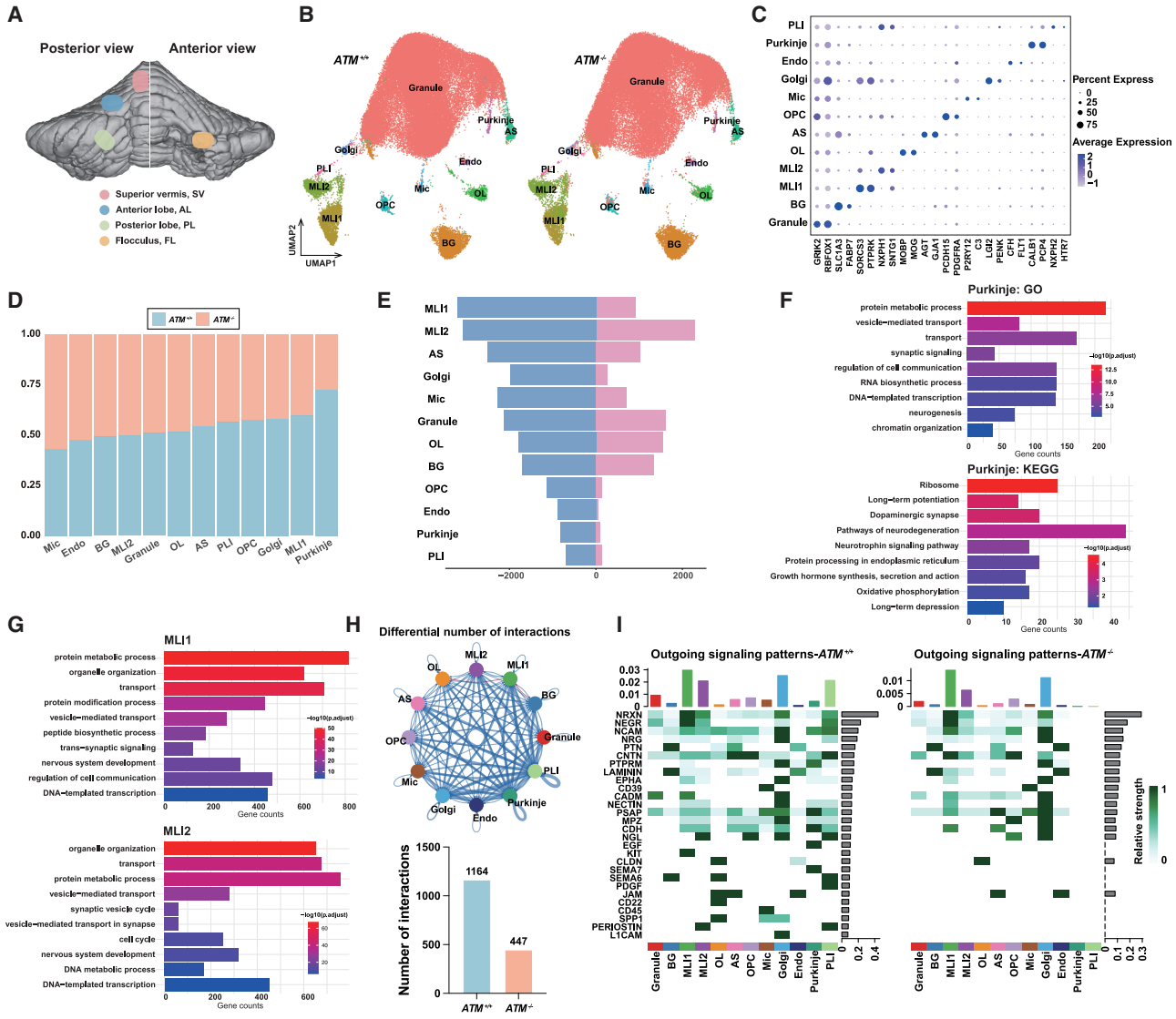

Figure 7. Single-cell transcriptomic atlas of neural cell types in the cerebellum of ATM-deficient and C1 macaques

(A) 3D visualization of all collected samples. A total of four cerebellar subregions (SV, AL, PL, and FL) were isolated and profiled using snRNA-seq.

(B) UMAP visualization of snRNA-seq profiles for all cell types, with colors representing different cell populations. AS, astrocyte; Endo, endothelial cell; Mic, microglia; MLI, molecular layer interneuron; PLI, Purkinje layer interneuron; OL, oligodendrocyte; OPC, oligodendrocyte precursor cell; BG, Bergmann glia; Granule, granule neuron; Golgi, Golgi neuron; Purkinje, Purkinje cell.

(C) Expression patterns of cell-type-specific markers from the snRNA-seq data shown in (B).

(D) Relative proportions of each cell type in control (C1; $ATM^{+/+}$) and ATM-deficient (A1; $ATM^{-/-}$) cerebellums following dataset integration.

(E) Gene ontology (GO) (*top*) and Kyoto encyclopedia of genes and genomes (KEGG) (*bottom*) terms associated with downregulated expressed genes in Purkinje cells of ATM-deficient cerebellum (A1). The length of the bar chart represents the number of genes, and the color indicates −log10(*p*.adjust) values.

(F) Differentially expressed genes (DEGs) between ATM-deficient (A1) and control (C1) macaques across various cell types. Blue bars represent down-regulated genes while pink bars represent up-regulated genes in ATM-deficient macaque (A1) relative to control according to the criteria |log2FoldChange| > 0, *p* value ≤0.05.

(G) GO terms associated with downregulated genes in MLI1 (*top*) and MLI2 (*bottom*) in ATM-deficient macaque (A1). The size of each point reflects the number of genes, and the color denotes −log10 (*p*.adjust) values.

(H) Overview of the intercellular communication networks among cells measured by network centrality analysis. Different cell populations are illustrated with different colors, and the blue edge represents a decrease in the number of interactions in ATM-deficient cerebellum compared with C1 (*top*). Decrease in the number of interactions among the cells in ATM-deficient cerebellum (A1) relative to C1 (*bottom*).

(I) Heatmaps of the overall signaling flows for each cell population mediated by individual signaling axes in ATM-deficient cerebellum (A1) and control (C1).

and 59,370 cells from the ATM-deficient macaque(A1), providing a balanced representation of both conditions (Figure 7B). Next, we employed a sophisticated bioinformatics pipeline to integrate the high-quality single-nucleus transcriptomic profiles from both macaques. This integration step was essential to minimize batch effects and enable direct comparisons between the two conditions. We then applied a global-scaling normalization method,[78–80] which normalizes feature expression for each cell based on its total expression, followed by the identification of highly variable features. A linear transformation was used to scale the dataset. Next, dimensionality reduction was performed using principal component analysis and uniform manifold approximation and projection (UMAP), allowing for visualization of the cellular landscape. These techniques project cells with similar gene expression profiles into a lower-dimensional space by capturing the underlying structure of the dataset (Figure 7B). Unsupervised clustering analysis was then applied to identify distinct cell populations based on their gene expression profiles. To annotate these clusters, we leveraged classical gene markers as described in recent literature, particularly drawing from the comprehensive study.[81] This approach enabled us to confidently define twelve distinct cell types within the cerebellum, including but not limited to Purkinje cells, granule cells, Golgi cells, stellate/basket cells, and various glial cell types (Figure 7C).

One of the most striking findings from our analysis was the marked reduction in the proportion of Purkinje cells in the ATM-deficient macaque (A1) compared to the control (C1), providing strong evidence of Purkinje cell loss (Figure 7D). This observation is particularly significant given the essential role of Purkinje cells in cerebellar function and motor coordination. In contrast, the proportions of most other cell types remained relatively stable between the two conditions, suggesting a selective vulnerability of Purkinje cells to ATM deficiency. To further investigate this phenomenon, we conducted differential gene expression analysis between Purkinje cells from ATM-deficient and control cerebella. Somewhat unexpectedly, Purkinje cells, despite their known susceptibility in A-T, exhibited only a small number of differentially expressed genes (DEGs) (Figure 7E; Table S3). This finding suggests that the observed reduction in Purkinje cell numbers may not stem from widespread transcriptional alterations within these cells, but rather from other factors such as increased susceptibility to apoptosis or disruptions in the local microenvironment. Nonetheless, several dysregulated pathways were identified, including those involved in synaptic plasticity, protein metabolism, and signal transmission (Figure 7F).

Additionally, we performed a comprehensive differential gene expression analysis across twelve distinct cell types identified in our snRNA-seq dataset, comparing the ATM-deficient (A1) and control (C1) conditions. Using a threshold of $|\log_2\text{FoldChange}| > 0$ and $p \leq 0.05$, we identified DEGs across these populations. This analysis revealed a striking and consistent pattern: all cell types predominantly exhibited downregulated gene expression in the ATM-deficient macaque (A1) relative to the control (C1). The most pronounced transcriptomic alterations were observed in two subtypes of molecular layer interneurons (MLIs), designated MLI1 and MLI2 (Figure 7F), which displayed the highest number of DEGs among all analyzed cell types. MLIs, comprising stellate and basket cells, are integral components of the cerebellar circuitry. They play critical roles in modulating Purkinje cell activity, maintaining cerebellar signaling fidelity, and providing trophic support to other cerebellar neurons.[41]

To better understand the functional implications of the observed gene expression changes in MLI1 and MLI2, we conducted gene set enrichment analysis on the downregulated genes. This analysis revealed significant enrichment of pathways related to protein metabolism, synaptic vesicle cycling, and neurotransmitter release (Figures 7G and S7C). These disruptions suggest that the functional capacity of MLIs to regulate cerebellar circuit activity may be compromised, potentially leading to impaired synaptic transmission and disrupted cerebellar homeostasis.

As Purkinje cell loss and MLIs dysfunction in the cerebellum significantly correlate with the pathological progression of ATM-deficient cerebellum, we conducted a cell-cell communication analysis to map coordinated differences in the cerebellar cellular communications underlying the ATM-deficient and healthy control conditions. We compared the global communication atlas between ATM-deficient (A1) and control (C1) cerebellums. We found that the total inferred interactions between cells decreased in the ATM-deficient cerebellum in terms of both the number and strength of the interactions (Figures 7H and S7D). Information flow analysis revealed that the epidermal growth factor (EGF), CD117, semaphorin 7A (SEMA7), semaphorin 6 (SEMA6), platelet-derived growth factor (PDGF), CD45, CD22, secreted phosphoprotein 1 (SPP1), PERIOSTIN, and L1 cell adhesion molecule (L1CAM) signaling pathways were switched off in the ATM-deficient cerebellum (Figure S7E). Then, we detected 28 signaling pathways among the 12-cell populations to distinguish the greatly altered signaling pathways in the ATM-deficient cerebellum (Figure 7I). Surprisingly, nearly all the signaling patterns were decreased in Purkinje cells and PLIs.

ATM kinase plays a crucial role in the DNA damage response pathway.[82–84] The signal network analysis reveals that ATM deficiency directly alters the expression pattern of several other important regulators and sensors including DNA mismatch repair proteins (MSH2 and MSH6), MRE11-RAD50-NBN (MRN) complex, tumor antigen p53 (TP53), serine/threonine-protein kinase ATR, mediator of DNA damage checkpoint protein 1, TP53-binding protein 1 (TP53BP1), serine/threonine-protein kinase CHEK2, and breast cancer type 1 susceptibility protein (BRCA1).[85–89] These alterations in the broader DNA damage response network highlight the central role of ATM and underscore the complex interdependencies within this cellular pathway (Figure S7F). These findings suggest that neurodegeneration changes in ATM-deficient cerebellum is a disease involving multiple cells and their interactions, rather than just Purkinje cell death or other single types of cellular dysfunction.

DISCUSSION

A-T is a complex genetic disorder associated with mutations in the *ATM* gene, which lead to a wide range of clinical symptoms including progressive neurological degeneration, immunodeficiency, and heightened cancer susceptibility.[1,5,73] Neuropathologically, A-T is characterized by neurodegenerative changes

that significantly impact cerebellar structures, particularly Purkinje and granule cells.[4,90] Several rodent models of A-T have been produced, and while they are by a large accurate genocopies of the disease, they have failed to replicate most of the neurological and neuropathological symptoms found in human A-T. Thus, advanced disease models are essential to mirror the relentless neurodegeneration of A-T and enable mechanistic and translational research.

In this study, a CRISPR-Cas9-engineered ATM-deficient rhesus macaque model, which overcomes several critical shortcomings of rodent models, was successfully generated. This NHP system more faithfully mimics the clinical and pathological progression of human A-T, particularly regarding cerebellar degeneration. ATM deficiency was confirmed through genetic and functional analyses in three macaques, all of which developed hallmark features of A-T, including elevated AFP, conjunctival telangiectasias, and hypersensitivity to radiation-induced DNA damage.[62,91] Importantly, the model displayed progressive neurodegeneration in a primate-specific anatomical context, underscoring the translational potential of NHPs for modeling complex neurodegenerative processes.[33,92–95]

Longitudinal multimodal analyses including molecular assays, MRI brain imaging, and behavioral testing revealed significant cerebellar atrophy localized to the vermis and hemispheres, with relatively preserved volumes in the cerebral cortex and hippocampus. This cerebellar-specific degeneration correlated with early-onset motor dysfunction (e.g., ataxic gait and stance), phenocopying human A-T.[62,91] By six months, ocular bulbar telangiectasias emerged, a defining clinical marker of A-T, and accompanied by systemic symptoms such as growth retardation, immune dysregulation, and elevated AFP levels.[8] Histological analyses confirmed early Purkinje cell loss, indicating that cerebellar degeneration initiates early in disease development.

To elucidate the molecular underpinnings of cerebellar dysfunction, we performed snRNA-seq on over 121,000 cerebellar cells. Twelve distinct cell types were identified, including a substantial reduction in Purkinje cells in ATM-deficient animals. Although most cell types exhibited global transcriptional downregulation, Purkinje cells showed surprisingly few DEGs. In contrast, MLIs (MLI1 and MLI2), which modulate cerebellar circuitry and provide critical support for Purkinje cells,[41] exhibit pronounced transcriptional suppression. Gene enrichment analyses revealed downregulation of pathways involved in translation and transcription, particularly eukaryotic initiation factors and ribosomal proteins, suggesting impaired protein synthesis and neuronal support. These changes may contribute to Purkinje cell vulnerability and dysfunction. Furthermore, spatial transcriptomic analyses have identified primate-specific subtypes of Purkinje cells and MLIs, characterized by distinct gene expression profiles and functional connectivity.[38] These findings point to evolutionarily conserved mechanisms that may underlie species-specific patterns of cerebellar degeneration and highlight the necessity of primate models for accurately capturing human A-T pathology.

In summary, this ATM-deficient macaque model faithfully recapitulates the neurodevelopmental, neurodegenerative, and systemic features of A-T, bridging a long-standing gap between murine models and human disease. The identification of primate-specific cellular and molecular signatures offers insights into A-T pathogenesis and establishes a robust platform for therapeutic discovery. Future studies leveraging this model to evaluate targeted therapies or gene therapy strategies could significantly advance treatment development for A-T and related cerebellar disorders.

Limitations of the study

We developed ATM-deficient macaques that mimic early-stage features of human A-T, including motor deficits, cerebellar atrophy, and altered cerebellar gene expression. However, a key limitation is the current focus on early manifestations. Understanding the full course of A-T will require longitudinal studies capturing late-stage phenotypes and broader systemic dysfunction, including the deep cerebellar nuclei, other brain regions, spinal cord, immune system, tumor susceptibility, and reproductive health. Additionally, due to model availability and ethical considerations, pathological and snRNA-seq analysis were conducted at a single time point and restricted to male macaques. This might preclude assessment of age- and sex-dependent pathophysiological variations in A-T progression. While we observed transcriptomic changes across cerebellar cell types, the mechanisms underlying Purkinje cell vulnerability remain unclear. Future work should dissect ATM-dependent DNA repair, metabolic regulation, oxidative stress pathways, and electrophysiological properties in specific neuronal and glial populations to identify targets for preventing motor decline.

The rarity of A-T presents challenges for therapy development and biomarker validation, underscoring the value of robust preclinical models. Despite the limited number of surviving ATM-deficient macaques, this model lays essential groundwork for large-scale phenotypic screens and therapeutic discovery. Finally, the absence of high-throughput, clinically translatable readouts—such as serum biomarkers or non-invasive imaging—limits the bridge to human applications. Future studies should prioritize scalable, cross-species assays to enhance translational potential.

RESOURCE AVAILABILITY

Lead contact

Further information and requests for resources and reagents should be directed to and will be fulfilled by the lead contact, Jiali Li (jiali.li@hmhn.org).

Materials availability

This study did not generate new unique reagents.

Data and code availability

- Single-nucleus RNA-seq data have been deposited in the National Genomics Data Center under the GSA code GSA: CRA018614 (https://ngdc.cncb.ac.cn/gsa/search?searchTerm=CRA018614) and are publicly available as of the date of publication.
- This paper does not report the original code.
- Any additional information required to reanalyze the data reported in this paper is available from the lead contact upon request.

ACKNOWLEDGMENTS

We would like to thank the National Research Facility of Phenotypic & Genetic Analysis of Model Animals (Primate Facility) (http://cstr.cn/31137.02.NPRC) and the Institutional Center for Shared Technologies and Facilities of Kunming

Institute of Zoology (KIZ), Chinese Academy of Sciences (CAS) for providing support in animal housing and care and technical assistance. Our appreciation goes to Yijiang Li, Chao Liu, Wenxian Xiao, Yun Wang, Lifen Xie, and Jiaqi Chen for their assistance with monkey maintenance and care. We are also grateful to Yingqi Guo and Xingcai Wu for their help in making EM samples and taking/analyzing EM images and Huanzhi Chen, Nanhui Chen, Jian Li, and Cong Li for their help in MRI scanning. We acknowledge Jing Wu and Zheng Bo for assisting in animal experiments and Xian-Tian Hu for valuable advice. We appreciate Siling Liu, Zhongyu Zhang, Wandi Xiong, and Rui Bi for early project discussions. This work was supported by grants from the Ministry of Science and Technology (China) of China (STI2030-Major Project 2021ZD0200900, 2022YFF0710900, and 2015CB755605), the National Natural Science Foundation of China (91649119, 92049105, and 82401697), Yunnan Province (E039030401, 202401AT070259, 202305AH340006, and 202305AF150160), CAS Special Research Assistant Project, Academician Expert Workstation of Yunnan Kunming (YSZJGZZ-2022063), and the CAS Light of West China Program (xbzg-zdsys-202213).

AUTHOR CONTRIBUTIONS

J.L., K.X., and Y.Z. provided the conceptual framework for this project and oversaw the execution of the experiments in their entirety. Yu Li, X.H., Z. Hu., and P.Z. performed embryo manipulation. K.X., X.Z., Y.Z., and L.L. performed an MRI scan and analyzed the data. K.X., Y.Z., Z. He., W.J., and Yanyan Li performed behavioral experiments. K.X., Y.Z., and Yifan Li performed molecular and pathological experiments. Y.C., M.Y., and D.-D.W. performed snRNA-seq and analyzed the data. D.J., X.Y., D.-F.Z., K.H., P.Z., and Y.-G. Y. provided technical and resource support in the experiments and financially supported this project. K.X., Y.Z., and J.L. wrote the manuscript. K.X., Y.Z., D. J., K.H., P.Z., Y.-G.Y., D.-D.W., and J. L. contributed to reviewing and editing the manuscript. J.L. supervised the project.

DECLARATION OF INTERESTS

The authors declare no competing interests.

STAR★METHODS

Detailed methods are provided in the online version of this paper and include the following:

SUPPLEMENTAL INFORMATION

Supplemental information can be found online at https://doi.org/10.1016/j.xcrm.2025.102355.

Received: October 29, 2024
Revised: May 11, 2025
Accepted: August 14, 2025
Published: September 16, 2025

REFERENCES

1. Boder, E. (1975). Ataxia-telangiectasia: some historic, clinical and pathologic observations. Birth Defects Orig. Artic. Ser. *11*, 255–270.
2. Swift, M., Morrell, D., Massey, R.B., and Chase, C.L. (1991). Incidence of cancer in 161 families affected by ataxia-telangiectasia. N. Engl. J. Med. *325*, 1831–1836.
3. Ambrose, M., and Gatti, R.A. (2013). Pathogenesis of ataxia-telangiectasia: the next generation of ATM functions. Blood *121*, 4036–4045.
4. McKinnon, P.J. (2012). ATM and the molecular pathogenesis of ataxia telangiectasia. Annu. Rev. Pathol. *7*, 303–321.
5. Sedgwick, R.P., and Boder, E. (1960). Progressive ataxia in childhood with particular reference to ataxia-telangiectasia. Neurology *10*, 705–715.
6. Lavin, M.F. (2008). Ataxia-telangiectasia: from a rare disorder to a paradigm for cell signalling and cancer. Nat. Rev. Mol. Cell Biol. *9*, 759–769.
7. Amirifar, P., Ranjouri, M.R., Lavin, M., Abolhassani, H., Yazdani, R., and Aghamohammadi, A. (2020). Ataxia-telangiectasia: epidemiology, pathogenesis, clinical phenotype, diagnosis, prognosis and management. Expert Rev. Clin. Immunol. *16*, 859–871.
8. Dineen, R.A., and Whitehouse, W.P. (2023). Ataxia Telangiectasia. In Essentials of Cerebellum and Cerebellar Disorders: A Primer For Graduate Students, D.L. Gruol, N. Koibuchi, M. Manto, M. Molinari, J.D. Schmahmann, and Y. Shen, eds. (Springer International Publishing), pp. 621–630.
9. Lee, J.H., and Paull, T.T. (2021). Cellular functions of the protein kinase ATM and their relevance to human disease. Nat. Rev. Mol. Cell Biol. *22*, 796–814.
10. Savitsky, K., Bar-Shira, A., Gilad, S., Rotman, G., Ziv, Y., Vanagaite, L., Tagle, D.A., Smith, S., Uziel, T., Sfez, S., et al. (1995). A single ataxia telangiectasia gene with a product similar to PI-3 kinase. Science *268*, 1749–1753.
11. Lavin, M.F., and Shiloh, Y. (1997). The genetic defect in ataxia-telangiectasia. Annu. Rev. Immunol. *15*, 177–202.
12. Marechal, A., and Zou, L. (2013). DNA damage sensing by the ATM and ATR kinases. Cold Spring Harb Perspect Biol *5*, a012716.
13. Matsuoka, S., Ballif, B.A., Smogorzewska, A., McDonald, E.R., 3rd, Hurov, K.E., Luo, J., Bakalarski, C.E., Zhao, Z., Solimini, N., Lerenthal, Y., et al. (2007). ATM and ATR substrate analysis reveals extensive protein networks responsive to DNA damage. Science *316*, 1160–1166.
14. Paull, T.T. (2015). Mechanisms of ATM Activation. Annu. Rev. Biochem. *84*, 711–738.
15. Zhang, J., Tripathi, D.N., Jing, J., Alexander, A., Kim, J., Powell, R.T., Dere, R., Tait-Mulder, J., Lee, J.H., Paull, T.T., et al. (2015). ATM functions at the peroxisome to induce pexophagy in response to ROS. Nat. Cell Biol. *17*, 1259–1269.

16. Guo, Z., Kozlov, S., Lavin, M.F., Person, M.D., and Paull, T.T. (2010). ATM activation by oxidative stress. Science *330*, 517–521. https://doi.org/10.1126/science.1192912.

17. Jiang, D., Zhang, Y., Hart, R.P., Chen, J., Herrup, K., and Li, J. (2015). Alteration in 5-hydroxymethylcytosine-mediated epigenetic regulation leads to Purkinje cell vulnerability in ATM deficiency. Brain *138*, 3520–3536.

18. Li, J., Chen, J., Ricupero, C.L., Hart, R.P., Schwartz, M.S., Kusnecov, A., and Herrup, K. (2012). Nuclear accumulation of HDAC4 in ATM deficiency promotes neurodegeneration in ataxia telangiectasia. Nat. Med. *18*, 783–790.

19. Li, J., Hart, R.P., Mallimo, E.M., Swerdel, M.R., Kusnecov, A.W., and Herrup, K. (2013). EZH2-mediated H3K27 trimethylation mediates neurodegeneration in ataxia-telangiectasia. Nat. Neurosci. *16*, 1745–1753.

20. Lee, J.H. (2024). Oxidative stress and the multifaceted roles of ATM in maintaining cellular redox homeostasis. Redox Biol. *75*, 103269.

21. Shiloh, Y. (2003). ATM and related protein kinases: safeguarding genome integrity. Nat. Rev. Cancer *3*, 155–168.

22. Cheng, A., Tse, K.H., Chow, H.M., Gan, Y., Song, X., Ma, F., Qian, Y.X.Y., She, W., and Herrup, K. (2021). ATM loss disrupts the autophagy-lysosomal pathway. Autophagy *17*, 1998–2010.

23. Chow, H.M., Shi, M., Cheng, A., Gao, Y., Chen, G., Song, X., So, R.W.L., Zhang, J., and Herrup, K. (2019). Age-related hyperinsulinemia leads to insulin resistance in neurons and cell-cycle-induced senescence. Nat. Neurosci. *22*, 1806–1819.

24. Aguado, J., Gómez-Inclán, C., Leeson, H.C., Lavin, M.F., Shiloh, Y., and Wolvetang, E.J. (2022). The hallmarks of aging in Ataxia-Telangiectasia. Ageing Res. Rev. *79*, 101653.

25. Kuhn, K., Lederman, H.M., and McGrath-Morrow, S.A. (2023). Ataxia-telangiectasia clinical trial landscape and the obstacles to overcome. Expert Opin. Investig. Drugs *32*, 693–704.

26. Zielen, S., Crawford, T., Benatti, L., Magnani, M., Kieslich, M., Ryan, M., Meyts, I., Gulati, S., Borgohain, R., Yadav, R., et al. (2024). Safety and efficacy of intra-erythrocyte dexamethasone sodium phosphate in children with ataxia telangiectasia (ATTeST): a multicentre, randomised, double-blind, placebo-controlled phase 3 trial. Lancet Neurol. *23*, 871–882.

27. Lavin, M.F. (2013). The appropriateness of the mouse model for ataxia-telangiectasia: neurological defects but no neurodegeneration. DNA Repair *12*, 612–619.

28. Tal, E., Alfo, M., Zha, S., Barzilai, A., De Zeeuw, C.I., Ziv, Y., and Shiloh, Y. (2018). Inactive Atm abrogates DSB repair in mouse cerebellum more than does Atm loss, without causing a neurological phenotype. DNA Repair *72*, 10–17.

29. Barlow, C., Hirotsune, S., Paylor, R., Liyanage, M., Eckhaus, M., Collins, F., Shiloh, Y., Crawley, J.N., Ried, T., Tagle, D., and Wynshaw-Boris, A. (1996). Atm-deficient mice: a paradigm of ataxia telangiectasia. Cell *86*, 159–171.

30. Campbell, A., Krupp, B., Bushman, J., Noble, M., Pröschel, C., and Mayer-Pröschel, M. (2015). A novel mouse model for ataxia-telangiectasia with a N-terminal mutation displays a behavioral defect and a low incidence of lymphoma but no increased oxidative burden. Hum. Mol. Genet. *24*, 6331–6349.

31. Perez, H., Abdallah, M.F., Chavira, J.I., Norris, A.S., Egeland, M.T., Vo, K.L., Buechsenschuetz, C.L., Sanghez, V., Kim, J.L., Pind, M., et al. (2021). A novel, ataxic mouse model of ataxia telangiectasia caused by a clinically relevant nonsense mutation. eLife *10*, e64695.

32. Zhou, Y., Sharma, J., Ke, Q., Landman, R., Yuan, J., Chen, H., Hayden, D.S., Fisher, J.W., Jiang, M., Menegas, W., et al. (2019). Atypical behaviour and connectivity in SHANK3-mutant macaques. Nature *570*, 326–331.

33. Pan, M.T., Zhang, H., Li, X.J., and Guo, X.Y. (2024). Genetically modified non-human primate models for research on neurodegenerative diseases. Zool. Res. *45*, 263–274.

34. Liu, Z., Li, X., Zhang, J.-T., Cai, Y.-J., Cheng, T.-L., Cheng, C., Wang, Y., Zhang, C.-C., Nie, Y.-H., Chen, Z.-F., et al. (2016). Autism-like behaviours and germline transmission in transgenic monkeys overexpressing MeCP2. Nature *530*, 98–102.

35. Liu, X., d'Oleire Uquillas, F., Viaene, A.N., Zhen, Z., and Gomez, J. (2022). A multifaceted gradient in human cerebellum of structural and functional development. Nat. Neurosci. *25*, 1129–1133.

36. Kebschull, J.M., Richman, E.B., Ringach, N., Friedmann, D., Albarran, E., Kolluru, S.S., Jones, R.C., Allen, W.E., Wang, Y., Cho, S.W., et al. (2020). Cerebellar nuclei evolved by repeatedly duplicating a conserved cell-type set. Science *370*, eabd5059.

37. Zhu, X., Yan, H., Zhan, Y., Feng, F., Wei, C., Yao, Y.G., and Liu, C. (2023). An anatomical and connectivity atlas of the marmoset cerebellum. Cell Rep. *42*, 112480.

38. Hao, S., Zhu, X., Huang, Z., Yang, Q., Liu, H., Wu, Y., Zhan, Y., Dong, Y., Li, C., Wang, H., et al. (2024). Cross-species single-cell spatial transcriptomic atlases of the cerebellar cortex. Science *385*, eado3927.

39. Aldinger, K.A., Thomson, Z., Phelps, I.G., Haldipur, P., Deng, M., Timms, A.E., Hirano, M., Santpere, G., Roco, C., Rosenberg, A.B., et al. (2021). Spatial and cell type transcriptional landscape of human cerebellar development. Nat. Neurosci. *24*, 1163–1175.

40. De Zeeuw, C.I., Lisberger, S.G., and Raymond, J.L. (2021). Diversity and dynamism in the cerebellum. Nat. Neurosci. *24*, 160–167.

41. Wu, T., Hu, E., Xu, S., Chen, M., Guo, P., Dai, Z., Feng, T., Zhou, L., Tang, W., Zhan, L., et al. (2021). clusterProfiler 4.0: A universal enrichment tool for interpreting omics data. Innovation *2*, 100141.

42. Chen, X., Du, Y., Broussard, G.J., Kislin, M., Yuede, C.M., Zhang, S., Dietmann, S., Gabel, H., Zhao, G., Wang, S.S.H., et al. (2022). Transcriptomic mapping uncovers Purkinje neuron plasticity driving learning. Nature *605*, 722–727.

43. Chen, Z., Zhang, R., Huo, H., Liu, P., Zhang, C., and Feng, T. (2022). Functional connectome of human cerebellum. Neuroimage *251*, 119015.

44. Dunbar, D.C., and Badam, G.L. (1998). Development of posture and locomotion in free-ranging primates. Neurosci. Biobehav. Rev. *22*, 541–546.

45. Hinde, K. (2009). Richer milk for sons but more milk for daughters: Sex-biased investment during lactation varies with maternal life history in rhesus macaques. Am. J. Hum. Biol. *21*, 512–519.

46. Golub, M.S., Keen, C.L., Gershwin, M.E., Styne, D.M., Takeuchi, P.T., Ontell, F., Walter, R.M., and Hendrickx, A.G. (1996). Adolescent growth and maturation in zinc-deprived rhesus monkeys. Am. J. Clin. Nutr. *64*, 274–282. [see comment].

47. Colman, R.J., Anderson, R.M., Johnson, S.C., Kastman, E.K., Kosmatka, K.J., Beasley, T.M., Allison, D.B., Cruzen, C., Simmons, H.A., Kemnitz, J.W., and Weindruch, R. (2009). Caloric restriction delays disease onset and mortality in rhesus monkeys. Science *325*, 201–204.

48. Huber, H.F., Ainsworth, H.C., Quillen, E.E., Salmon, A., Ross, C., Azhar, A.D., Bales, K., Basso, M.A., Coleman, K., Colman, R., et al. (2025). Comparative lifespan and healthspan of nonhuman primate species common to biomedical research. Geroscience *47*, 135–151.

49. Feng, G., Jensen, F.E., Greely, H.T., Okano, H., Treue, S., Roberts, A.C., Fox, J.G., Caddick, S., Poo, M.M., Newsome, W.T., and Morrison, J.H. (2020). Opportunities and limitations of genetically modified nonhuman primate models for neuroscience research. Proc. Natl. Acad. Sci. USA *117*, 24022–24031.

50. Schmidt, J.K., Jones, K.M., Van Vleck, T., and Emborg, M.E. (2022). Modeling genetic diseases in nonhuman primates through embryonic and germline modification: Considerations and challenges. Sci. Transl. Med. *14*, eabf4879.

51. Chen, Y., Zheng, Y., Kang, Y., Yang, W., Niu, Y., Guo, X., Tu, Z., Si, C., Wang, H., Xing, R., et al. (2015). Functional disruption of the dystrophin gene in rhesus monkey using CRISPR/Cas9. Hum. Mol. Genet. *24*, 3764–3774.

52. Ren, S., Fu, X., Guo, W., Bai, R., Li, S., Zhang, T., Liu, J., Wang, Z., Zhao, H., Suo, S., et al. (2024). Profound cellular defects attribute to muscular pathogenesis in the rhesus monkey model of Duchenne muscular dystrophy. Cell *187*, 6669–6686.

53. Li, M., Guan, M., Lin, J., Zhu, K., Zhu, J., Guo, M., Li, Y., Chen, Y., Chen, Y., Zou, Y., et al. (2024). Early blood immune molecular alterations in cynomolgus monkeys with a PSEN1 mutation causing familial Alzheimer's disease. Alzheimer's Dement. *20*, 5492–5510.

54. Zhang, W.H., Zhuang, J.H., Guo, Y.Y., Chen, X.Y., Li, Y.Q., Xu, J.Q., Zhang, A.R., Chen, B.Y., Meng, W., Zhu, Y.H., et al. (2024). Pancreatic agenesis and altered m6A methylation in the pancreas of PDX1-mutant cynomolgus macaques. Zool. Res. *45*, 1188–1200.

55. Bae, S., Park, J., and Kim, J.S. (2014). Cas-OFFinder: a fast and versatile algorithm that searches for potential off-target sites of Cas9 RNA-guided endonucleases. Bioinformatics *30*, 1473–1475.

56. Renaud, M., Tranchant, C., Koenig, M., and Anheim, M. (2020). Autosomal Recessive Cerebellar Ataxias With Elevated Alpha-Fetoprotein: Uncommon Diseases, Common Biomarker. Mov. Disord. *35*, 2139–2149.

57. Hoch, N.C., Hanzlikova, H., Rulten, S.L., Tétreault, M., Komulainen, E., Ju, L., Hornyak, P., Zeng, Z., Gittens, W., Rey, S.A., et al. (2017). XRCC1 mutation is associated with PARP1 hyperactivation and cerebellar ataxia. Nature *541*, 87–91.

58. van Os, N.J.H., Jansen, A.F.M., van Deuren, M., Haraldsson, A., van Driel, N.T.M., Etzioni, A., van der Flier, M., Haaxma, C.A., Morio, T., Rawat, A., et al. (2017). Ataxia-telangiectasia: Immunodeficiency and survival. Clin. Immunol. *178*, 45–55.

59. Graafen, L., Heinze, A., Albinger, N., Salzmann-Manrique, E., Ganß, F., Hünecke, S., Cappel, C., Wölke, S., Donath, H., Trischler, J., et al. (2024). Immune profiling and functional analysis of NK and T cells in ataxia telangiectasia. Front. Immunol. *15*, 1377955.

60. Zielen, S., Duecker, R.P., Woelke, S., Donath, H., Bakhtiar, S., Buecker, A., Kreyenberg, H., Huenecke, S., Bader, P., Mahlaoui, N., et al. (2021). Simple Measurement of IgA Predicts Immunity and Mortality in Ataxia-Telangiectasia. J. Clin. Immunol. *41*, 1878–1892.

61. Takada, S., Weitering, T.J., van Os, N.J.H., Du, L., Pico-Knijnenburg, I., Kuipers, T.B., Mei, H., Salzer, E., Willemsen, M.A.A.P., Weemaes, C.M.R., et al. (2024). Causative mechanisms and clinical impact of immunoglobulin deficiencies in ataxia telangiectasia. J. Allergy Clin. Immunol. *153*, 1392–1405.

62. Levy, A., and Lang, A.E. (2018). Ataxia-telangiectasia: A review of movement disorders, clinical features, and genotype correlations. Mov. Disord. *33*, 1238–1247.

63. Schon, K., van Os, N.J.H., Oscroft, N., Baxendale, H., Scoffings, D., Ray, J., Suri, M., Whitehouse, W.P., Mehta, P.R., Everett, N., et al. (2019). Genotype, extrapyramidal features, and severity of variant ataxia-telangiectasia. Ann. Neurol. *85*, 170–180.

64. Rao, J.S., Zhao, C., Zhang, A., Duan, H., Hao, P., Wei, R.H., Shang, J., Zhao, W., Liu, Z., Yu, J., et al. (2018). NT3-chitosan enables de novo regeneration and functional recovery in monkeys after spinal cord injury. Proc. Natl. Acad. Sci. USA *115*, E5595–E5604.

65. Shi, L., Luo, X., Jiang, J., Chen, Y., Liu, C., Hu, T., Li, M., Lin, Q., Li, Y., Huang, J., et al. (2019). Transgenic rhesus monkeys carrying the human MCPH1 gene copies show human-like neoteny of brain development. Natl. Sci. Rev. *6*, 480–493.

66. Funahashi, S. (2015). Functions of delay-period activity in the prefrontal cortex and mnemonic scotomas revisited. Front. Syst. Neurosci. *9*, 2.

67. Carlen, M. (2017). What constitutes the prefrontal cortex? Science *358*, 478–482.

68. Liu, Z., Li, X., Zhang, J.T., Cai, Y.J., Cheng, T.L., Cheng, C., Wang, Y., Zhang, C.C., Nie, Y.H., Chen, Z.F., et al. (2016). Autism-like behaviours and germline transmission in transgenic monkeys overexpressing MeCP2. Nature *530*, 98–102.

69. Nakagami, A., Yasue, M., Nakagaki, K., Nakamura, M., Kawai, N., and Ichinohe, N. (2022). Reduced childhood social attention in autism model marmosets predicts impaired social skills and inflexible behavior in adulthood. Front. Psychiatry *13*, 885433.

70. Dineen, R.A., Raschke, F., McGlashan, H.L., Pszczolkowski, S., Hack, L., Cooper, A.D., Prasad, M., Chow, G., Whitehouse, W.P., and Auer, D.P. (2020). Multiparametric cerebellar imaging and clinical phenotype in childhood ataxia telangiectasia. Neuroimage. Clin. *25*, 102110.

71. Paxinos, G., Huang, X.F., and Toga, A.W. (2000). The Rhesus Monkey Brain in Stereotaxic Coordinates (Academic Press).

72. Dudink, I., White, T.A., Ardalan, M., Mallard, C., Ballerin, G., Creed, S.J., Pham, Y., Sutherland, A.E., Castillo-Melendez, M., Allison, B.J., and Miller, S.L. (2022). An Optimized and Detailed Step-by-Step Protocol for the Analysis of Neuronal Morphology in Golgi-Stained Fetal Sheep Brain. Dev. Neurosci. *44*, 344–362.

73. Ouimet, C.C., LaMantia, A.S., Goldman-Rakic, P., Rakic, P., and Greengard, P. (1992). Immunocytochemical localization of DARPP-32, a dopamine and cyclic-AMP-regulated phosphoprotein, in the primate brain. J. Comp. Neurol. *323*, 209–218.

74. Cutando, L., Puighermanal, E., Castell, L., Tarot, P., Belle, M., Bertaso, F., Arango-Lievano, M., Ango, F., Rubinstein, M., Quintana, A., et al. (2022). Cerebellar dopamine D2 receptors regulate social behaviors. Nat. Neurosci. *25*, 900–911.

75. Hawkes, R., and Herrup, K. (1995). Aldolase C/zebrin II and the regionalization of the cerebellum. J. Mol. Neurosci. *6*, 147–158.

76. Lee, J.H., and Paull, T.T. (2020). Mitochondria at the crossroads of ATM-mediated stress signaling and regulation of reactive oxygen species. Redox Biol. *32*, 101511.

77. Ibrahim, M., Butt, A.M., and Berry, M. (1995). Relationship between myelin sheath diameter and internodal length in axons of the anterior medullary velum of the adult rat. J. Neurol. Sci. *133*, 119–127.

78. McGinnis, C.S., Murrow, L.M., and Gartner, Z.J. (2019). DoubletFinder: Doublet Detection in Single-Cell RNA Sequencing Data Using Artificial Nearest Neighbors. Cell Syst. *8*, 329–337.

79. Korsunsky, I., Millard, N., Fan, J., Slowikowski, K., Zhang, F., Wei, K., Baglaenko, Y., Brenner, M., Loh, P.R., and Raychaudhuri, S. (2019). Fast, sensitive and accurate integration of single-cell data with Harmony. Nat. Methods *16*, 1289–1296.

80. Kolberg, L., Raudvere, U., Kuzmin, I., Vilo, J., and Peterson, H. (2020). gprofiler2 – an R package for gene list functional enrichment analysis and namespace conversion toolset g:Profiler. F1000Res. *9*, ELIXIR-709.

81. Kozareva, V., Martin, C., Osorno, T., Rudolph, S., Guo, C., Vanderburg, C., Nadaf, N., Regev, A., Regehr, W.G., and Macosko, E. (2021). A transcriptomic atlas of mouse cerebellar cortex comprehensively defines cell types. Nature *598*, 214–219.

82. Blackford, A.N., and Jackson, S.P. (2017). ATM, ATR, and DNA-PK: The Trinity at the Heart of the DNA Damage Response. Mol. Cell *66*, 801–817.

83. Prasad, A., and Kanakkanthara, A. (2024). An ATM D-compartmentalization in DNA damage response. Trends Cell Biol. *34*, 173–175.

84. Cuella-Martin, R., Hayward, S.B., Fan, X., Chen, X., Huang, J.W., Taglialatela, A., Leuzzi, G., Zhao, J., Rabadan, R., Lu, C., et al. (2021). Functional interrogation of DNA damage response variants with base editing screens. Cell *184*, 1081–1097.

85. Jiang, M., Jia, K., Wang, L., Li, W., Chen, B., Liu, Y., Wang, H., Zhao, S., He, Y., and Zhou, C. (2021). Alterations of DNA damage response pathway: Biomarker and therapeutic strategy for cancer immunotherapy. Acta Pharm. Sin. B *11*, 2983–2994.

86. Wang, Y., and Qin, J. (2003). MSH2 and ATR form a signaling module and regulate two branches of the damage response to DNA methylation. Proc. Natl. Acad. Sci. USA *100*, 15387–15392.

87. Lou, Z., Minter-Dykhouse, K., Wu, X., and Chen, J. (2003). MDC1 is coupled to activated CHK2 in mammalian DNA damage response pathways. Nature *421*, 957–961.

88. Gupta, R., Somyajit, K., Narita, T., Maskey, E., Stanlie, A., Kremer, M., Typas, D., Lammers, M., Mailand, N., Nussenzweig, A., et al. (2018). DNA Repair Network Analysis Reveals Shieldin as a Key Regulator of NHEJ and PARP Inhibitor Sensitivity. Cell *173*, 972–988.

89. Karakostis, K., Malbert-Colas, L., Thermou, A., Vojtesek, B., and Fåhraeus, R. (2024). The DNA damage sensor ATM kinase interacts with the p53 mRNA and guides the DNA damage response pathway. Mol. Cancer *23*, 21.

90. Bundey, S. (1994). Clinical and genetic features of ataxia-telangiectasia. Int. J. Radiat. Biol. *66*, S23–S29.

91. van Os, N.J.H., Hensiek, A., van Gaalen, J., Taylor, A.M.R., van Deuren, M., Weemaes, C.M.R., Willemsen, M.A.A.P., and van de Warrenburg, B. P.C. (2019). Trajectories of motor abnormalities in milder phenotypes of ataxia telangiectasia. Neurology *92*, e19–e29.

92. Phillips, K.A., Bales, K.L., Capitanio, J.P., Conley, A., Czoty, P.W., t Hart, B.A., Hopkins, W.D., Hu, S.L., Miller, L.A., Nader, M.A., et al. (2014). Why primate models matter. Am. J. Primatol. *76*, 801–827.

93. Tarantal, A.F., Noctor, S.C., and Hartigan-O'Connor, D.J. (2022). Nonhuman Primates in Translational Research. Annu. Rev. Anim. Biosci. *10*, 441–468.

94. Yang, Y., Lu, X., Liu, N., Ma, S., Zhang, H., Zhang, Z., Yang, K., Jiang, M., Zheng, Z., Qiao, Y., et al. (2024). Metformin decelerates aging clock in male monkeys. Cell *187*, 6358–6378.

95. Li, H., Su, L.Y., Yang, L., Li, M., Liu, Q., Li, Z., Hu, Y., Li, H., Wu, S., Wang, W., et al. (2021). A cynomolgus monkey with naturally occurring Parkinson's disease. Natl. Sci. Rev. *8*, nwaa292.

96. Yushkevich, P.A., Piven, J., Hazlett, H.C., Smith, R.G., Ho, S., Gee, J.C., and Gerig, G. (2006). User-guided 3D active contour segmentation of anatomical structures: Significantly improved efficiency and reliability. Neuroimage *31*, 1116–1128.

97. Marcus, D.S., Harwell, J., Olsen, T., Hodge, M., Glasser, M.F., Prior, F., Jenkinson, M., Laumann, T., Curtiss, S.W., and Van Essen, D.C. (2011). Informatics and data mining tools and strategies for the human connectome project. Front. Neuroinform. *5*, 4.

98. Cox, R.W. (2012). AFNI: What a long strange trip it's been. Neuroimage *62*, 743–747.

99. Fischl, B. (2012). FreeSurfer. Neuroimage *62*, 774–781.

100. Hao, Y., Stuart, T., Kowalski, M.H., Choudhary, S., Hoffman, P., Hartman, A., Srivastava, A., Molla, G., Madad, S., Fernandez-Granda, C., and Satija, R. (2024). Dictionary learning for integrative, multimodal and scalable single-cell analysis. Nat. Biotechnol. *42*, 293–304.

101. Jin, S., Guerrero-Juarez, C.F., Zhang, L., Chang, I., Ramos, R., Kuan, C. H., Myung, P., Plikus, M.V., and Nie, Q. (2021). Inference and analysis of cell-cell communication using CellChat. Nat. Commun. *12*, 1088.

102. Qin, D.D., Zhou, J.K., He, X.C., Shen, X.Y., Li, C., Chen, H.Z., Yan, L.Z., Hu, Z.F., Li, X., Lv, L.B., et al. (2021). Depletion of giant ANK2 in monkeys causes drastic brain volume loss. Cell Discov. *7*, 113.

103. Rao, J.-S., Zhao, C., Zhang, A., Duan, H., Hao, P., Wei, R.-H., Shang, J., Zhao, W., Liu, Z., Yu, J., et al. (2018). NT3-chitosan enables de novo regeneration and functional recovery in monkeys after spinal cord injury. Proc. Natl. Acad. Sci. USA *115*, E5595–E5604.

104. Sugiyama, Y., Higo, N., Yoshino-Saito, K., Murata, Y., Nishimura, Y., Oishi, T., and Isa, T. (2013). Effects of early versus late rehabilitative training on manual dexterity after corticospinal tract lesion in macaque monkeys. J. Neurophysiol. *109*, 2853–2865.

105. Tustison, N., Avants, B., Cook, P., Kim, J., Whyte, J., Gee, J., Ahlers, S., and Stone, J. (2011). Multivariate Analysis of Diffusion Tensor Imaging and Cortical Thickness Maps in a Traumatic Brain Injury (Tbi) Cohort Using Advanced Normalization Tools (Ants). J Neurotraum *28*, A111.

106. Yu, Z., Han, X., Xu, W., Zhang, J., Marr, C., Shen, D., Peng, T., Zhang, X. Y., and Feng, J. (2022). A generalizable brain extraction net (BEN) for multimodal MRI data from rodents, nonhuman primates, and humans. eLife *11*, e81217.

107. Pang, J.C., Aquino, K.M., Oldehinkel, M., Robinson, P.A., Fulcher, B.D., Breakspear, M., and Fornito, A. (2023). Geometric constraints on human brain function. Nature *618*, 566–574.

108. Chen, A., Sun, Y., Lei, Y., Li, C., Liao, S., Meng, J., Bai, Y., Liu, Z., Liang, Z., Zhu, Z., et al. (2023). Single-cell spatial transcriptome reveals cell-type organization in the macaque cortex. Cell *186*, 3726–3743.

109. Ament, S.A., Cortes-Gutierrez, M., Herb, B.R., Mocci, E., Colantuoni, C., and McCarthy, M.M. (2023). A single-cell genomic atlas for maturation of the human cerebellum during early childhood. Sci. Transl. Med. *15*, eade1283.

STAR★METHODS

KEY RESOURCES TABLE

REAGENT or RESOURCE	SOURCE	IDENTIFIER
Antibodies		
Anti -CD3 Rabbit pAb	Servicebio	Cat# GB11014; RRID: AB_3083642
Anti -CD20 Rabbit pAb	Servicebio	Cat# GB11540 RRID: AB_3698721
Anti-DARPP-32 Rabbit mAb	Cell Signaling Technology	Cat# 2306; RRID: AB_2169007
Anti-ATM antibody	Abcam	Cat# Ab32420; RRID: AB_725574
Anti-PSD95 antibody	Invitrogen	Cat# MA1-046 RRID: AB_2092361
Anti-Synapsin I antibody	Abcam	Cat# Ab64581; RRID: AB_1281135
Anti-PARP antibody	Cell Signaling Technology	Cat# 9542; RRID: AB_2160739
Anti-Aldoc antibody	Oasis biofarm	Cat# OB-PRT030; RRID: AB_2938960
Anti-Cleaved Caspase-3	Cell Signaling Technology	Cat# 9661; RRID: AB_2341188
Anti-Iba1 antibody	Wako	Cat# 019–19741; RRID: AB_839504
Anti-GFAP antibody	Abcam	Cat# Ab254083 RRID: AB_3698724
Anti-beta Actin antibody	Abcam	Cat# Ab8226; RRID: AB_306371
Anti-GAPDH antibody [6C5]	Abcam	Cat# Ab8245; RRID: AB_2107448
Goat anti-mouse IgG (H + L) secondary antibody, HRP	Invitrogen	Cat# 31430; RRID: AB_228307
Goat anti-Rabbit IgG (H + L) cross-adsorbed secondary antibody, HRP	Invitrogen	Cat# G-21234; RRID: AB_1500696
Bacterial and virus strains		
Trelief 5α Chemically Competent Cell	TSINGKE	Cat# TSC-C01
Chemicals, peptides, and recombinant proteins		
Recombinant human follitropin alpha (r-hFSH)	Merck Serono	Cat# AU026521
Recombinant human chorionic gonadotropin alpha (rHCG)	Merck Serono	Cat# BA054379
TrueCutTM Cas9 Protein v2	Invitrogen	Cat# A36496
Etoposide	Sigma	Cat# E1383
Proteinase K	Roche	Cat# 15891840
Dulbecco's Modification of Eagle's Medium (DMEM)	Gibco	Cat# 12430054
Dulbecco's Modified Eagle Medium/ Nutrient Mixture F-12 (DMEM/F12)	Gibco	Cat# 11320033
Fetal Bovine Serum (FBS)	Gibco	Cat# 10091148
Trypsin-EDTA	Gibco	Cat# 25200072
GlutaMAX	Gibco	Cat# 35050061
37% formaldehyde	Sigma-Aldrich	Cat# F1635
BbsI-HF	NEB	Cat# R3539M
T4 DNA ligase	NEB	Cat# M0202
T4 DNA polymerase	NEB	Cat# M0203
Lipofectamine 3000	Thermo Fisher	Cat# L3000015
TRIzol reagent	Invitrogen	Cat# 15596026
PicoPure DNA Extraction Kit	Invitrogen	Cat# KIT0103
Hematoxylin-eosin (H&E) HD Constant Dye Kit	Servicebio	Cat# G1076
T-Vector pMD19	TaKaRa	Cat# 3271

(*Continued on next page*)

Continued

REAGENT or RESOURCE	SOURCE	IDENTIFIER
Ketamine hydrochloride	Gutian pharmaceutical	Cat# 1505242
Dexmedetomidine HCl	Aladdin	Cat# D129813
Critical commercial assays		
Rapid GolgiStain Kit	FD NeuroTechnologies	Cat# PK401
Annexin V FITC Apoptosis Kit	BD Biosciences	Cat# 556547
YF®488 TUNEL	Acros Organics	Cat# T6013S
Deposited data		
Raw data for snRNA-seq	This paper	GSA: CRA018614
Experimental models: Cell lines		
COS-7	Conservation Genetics CAS Kunming Cell Bank	Cat# KCB 93019YJ
Macaque skin fibroblasts	This study	N/A
Experimental models: Organisms/strains		
Rhesus macaques	Kunming Primate Research Center, Chinese Academy of Sciences	N/A
Oligonucleotides		
sgRNA1: UUGUUUCAGGAUCUCGAAUC	This study	N/A
sgRNA2: CGGCAUUCAGAUUCCAAACA	This study	N/A
mmATM-exon3 (forward): TGCTGCCGTCAACTAGAACA	This study	N/A
mmATM-exon3 (reverse): TGCCAAATTCATATGCAAGGCA	This study	N/A
Recombinant DNA		
PX459	Addgene	Addgene plasmid # 62988
Software and algorithms		
ImageJ	NIH	https://imagej.nih.gov/ij/
GraphPad Prism 9.0	GraphPad Software	https://www.graphpad.com/scientific-software/prism/
Adobe Illustrator	Adobe	https://www.adobe.com/products/illustrator.html
MATLAB version 2020a	MathWorks	https://www.mathworks.com
ITK-SNAP Version 3.8.0	Yushkevich et al.[96]	http://www.itksnap.org/pmwiki/pmwiki.php
Connectome Workbench Version 1.4.2	Marcus et al.[97]	https://www.humanconnectome.org/software/connectome-workbench
AFNI Version 22.1.10	Cox et al.[98]	https://afni.nimh.nih.gov/
Freesurfer Version 3.0	Fischl et al.[99]	https://surfer.nmr.mgh.harvard.edu/
R	R Core Team	https://www.r-project.org/
Python	Python Software Foundation	https://www.python.org/
Seurat v4.3.0.1	Hao et al.[100]	https://satijalab.org/seurat/
DoubletFinder v2.0.3	McGinnis et al.[78]	https://github.com/chris-mcginnis-ucsf/DoubletFinder
Harmony (v1.2.0)	Korsunsky et al.[79]	https://github.com/immunogenomics/harmony
Gprofiler2 (v0.2.3)	Kolberg et al.[80]	https://CRAN.R-project.org/package=gprofiler2
CellChat (v1.6.1)	Jin et al.[101]	https://github.com/sqjin/CellChat
Other		
Nuclear Magnetic Resonance Imaging	United Imaging	uMR770/3.0 T
Automatic blood cell analyzer (veterinary)	Mindray	BC-5000 Vet

(*Continued on next page*)

Continued

REAGENT or RESOURCE	SOURCE	IDENTIFIER
Automatic animal 3D gait analysis system	Kinema Tracer for Animal	Kinema Tracer for Animal
Automatic chemiluminescence image analysis system	Tanon	5200
X-ray irradiation instrument	Xstrahl	CIX3
Flow cytometer	BD Biosciences	LSR Fortessa
NanoDrop	Life technologies	ND-1000
Microscope slide scanner	Pannoramic	250 Flash III
Laser scanning confocal microscope	Olympus	FV1000

EXPERIMENTAL MODEL AND STUDY PARTICIPANT DETAILS

Ethical statement

All experimental processes in this study comply with the Animal Care and Use Institutional Committee of the Institutional Animal Care and Use Committee of Kunming Institute of Zoology (IACUC20005), Chinese Academy of Sciences (CAS).

Animals

Throughout the experiment, the rhesus macaque (Macaca mulatta) was housed in a conditioned environment (temperature: 22 ± 1°C, relative humidity: 50% ± 5%) with 12 h light/dark cycle. All animals were given a commercial monkey diet twice a day with tap water and were fed fruits and vegetables once daily. Routine veterinary care was provided by professional keepers and veterinarians during the entire process of experiments.

Cells

COS-7 cells (African Green Monkey Kidney Cell) were obtained from Conservation Genetics CAS Kunming Cell Bank and were cultured at 37°C with DMEM media (Corning), 10% Fetal Bovine Serum (FBS) (Gibco), and 100 U/mL penicillin-streptomycin (Gibco). Primary fibroblasts were derived from macaque ear skin and were cultured at 37°C with DMEM media (Corning), 10% FBS (Gibco), and 100 U/mL penicillin-streptomycin (Gibco).

METHOD DETAILS

Preparation of gRNAs

The sgRNAs that target the *ATM* exon (designed using Guide Design Tools (https://www.zlab.bio/resources)) were inserted into the pSpCas9(BB)-2A-Puro (PX459) vector and the constructed plasmids were transfected into COS-7 cells, followed by flow cytometry sorting (Beckman). Genomic DNA of green fluorescent positive cells was extracted to verify the knockout efficiency (using PCR and Sanger sequencing).

RNP preparation

Guide RNA1 5′-UUGUUUCAGGAUCUCGAAUCGUUUUAGAGCUAGAAAUAGCAAGUUAAAAUAAGGCUAGUCCGUUAUCAACUU GAAAAAGUGGCACCGAGUCGGUGCUUUU-3′ and guide RNA2 5′-CGGCAUUCAGAUUCCAAACAGUUUUAGAGCUAGAAAUAG CAAGUUAAAAUAAGGCUAGUCCGUUAUCAACUUGAAAAAGUGGCACCGAGUCGGUGCUUUU-3′ were obtained from GenScript, with the target RNA underlined. Cas9 protein was obtained from Invitrogen. In the preparation of ribonucleoprotein (RNP), the final concentration of single sgRNA was 133 ng/μL, and the final concentration of Cas9 protein was 300 ng/μL.

Oocyte collection and *in vitro* fertilization

Oocyte collection and fertilization were performed as previously described.[102] In brief, 3 healthy female cynomolgus monkeys aged 5–8 years with regular menstrual cycles were selected as oocyte donors for superovulation, which was performed by intramuscular injection with rhFSH (recombinant human follitropin alpha, GONAL-F, Merck Serono) for 8 days, then rhCG (recombinant human chorionic gonadotropin alpha, OVIDREL, Merck Serono) on day 9 Oocytes were collected by laparoscopic follicular aspiration 32 h after rhCG administration. Follicular contents were placed in Hepes-buffered Tyrode's albumin lactate pyruvate medium containing 0.3% BSA at 37°C. Oocytes were stripped of cumulus cells by pipetting after a brief exposure (<1 min) to hyaluronidase (0.5 mg/mL) in TALP-Hepes to allow visual selection of nuclear maturity metaphase II (MII; first polar body present) oocytes. The maturity oocytes were subjected to intracytoplasmic sperm injection (ICSI) immediately and then cultured in CMRL-1066 containing 10% FBS at 37°C in 5% CO_2. Fertilization was confirmed by the presence of the second polar body and two pronuclei.

Genotyping of mutant monkeys

To genotype ATM mutation in newborn macaques, a PCR product flanking the desired mutation site was amplified using high-fidelity polymerase from blood and skin genomic DNA of all macaques, using primer forward: 5′-TGCTGCCGTCAACTAGAACA-3′ and reverse: 5′-TGCCTTGCATATGAATTTGGCA-3′. PCR products from individual macaques were TA-cloned into T-vector (Takara). Ligation mixtures were transformed into competent Escherichia coli and plated onto plates with ampicillin selectivity. Individual bacterial colonies were picked up, and plasmid DNA was subjected to Sanger sequencing using M13 primer to examine various types of indels and their percentages.

Fibroblast isolation and cell culture

The macaque skin obtained from the ear rim was disinfected with 75% ethanol, hair and fat tissue were removed, washed with PBS, and then cut into small pieces and pasted on a Petri dish. Fibroblasts can be grown within a week. All cells were cultured in DMEM high-glucose (Corning) medium containing 10% FBS (Gibco), 1% glutamine (Gibco), and 1% penicillin/streptomycin (Gibco). Culture at 37°C in 5% CO_2.

Blood analysis

Before feeding in the morning, a professional veterinarian collected fresh whole blood from the monkeys' upper arms. Whole blood was immediately used for routine blood analysis after EDTA anticoagulation, and supernatant was centrifuged for alpha-fetoprotein and immunoassay.

Behavior observation and analysis

Behavioral observation and analysis were performed by two independent trained observers with at least 80% inter-observer reliability. None of the observers knew the genotype of the macaques.

Analysis of locomotive behaviors

The monkeys were observed alone in observation cages after weaning. The observation cage is similar to their home cage.[34] All motion behaviors were recorded continuously for 20 min every day, and all data were summarized to calculate the time distribution of the range of motion in the cage and the scope of exploration.

Kinematics analyses of bipedal locomotion

The bipedal movement of animals was characterized by gait test and footprints. In a nutshell, each group of monkeys (n = 3) performed bipedal exercise on a treadmill under restricted conditions with a customized device.[103] After the macaques acclimated (without biting the traction bar or making strange noises), the macaques were pulled to the treadmill for acclimation training at a starting speed of 0.8 km/h. After running for 30 s in the first phase, the macaques were allowed to rest for 1–2 min and given a food reward. The treadmill speed was adjusted to 1 km/h, 2 km/h or 3 km/h according to the animal adaptation state, but in actual operation, it was found that some AT groups could not adapt to the speed of 3 km/h and above. Therefore, the subsequent fixed training speed was 1 km/h, 2 km/h, and 3 km/h, that is, each monkey trained three times a day. After 30 days of training, they can adapt to the treadmill, eat the reward normally when resting, and do not become overly anxious when they return to the cage. After dipping the monkey's feet in diluted food coloring during the trail, the treadmill was turned on, and the monkey walked on the treadmill and recorded its gait. Limb and joint movements were recorded by four cameras connected to the Kinema Tracer for Animal automated 3D Animal Gait Analysis system. Gait data, including stride length, stride width, stride frequency and gait period, are recorded by measuring distance. Obtain data for successive steps for subsequent processing and analysis. The kinematic analysis was as follows: (i) food coloring was used to label both sides of the macaque's joints, including the toe joints, ankle joints, knee joints, hip joints, and sacroiliac joints; (ii) gait datasets were calculated using MATLAB (MathWorks, Natick, MA, USA). The parameters of each gait cycle (including feature parameters and correlation coefficients) were extracted and normalized; (iii) 3D reconstruction 121, collecting 20–30 consecutive gait cycles, and analyzing the locomotion gait of monkeys. All parameter data of the three groups were analyzed and displayed.

Manual dexterity training and testing

Monkeys were trained on manual dexterity with a Klüver board, which contains cylindrical wells of five different sizes (10, 10.5, 11, 12, and 13 mm in diameter, 7 mm in depth).[104] In the Klüver board task, the board was placed on the floor in front of the cage, and monkeys retrieved small spherical food pellets (3 mm in diameter) from the wells. Monkeys were trained to retrieve the food pellets from one of the five wells of different sizes for 30 min/day and 5 days/wk. On the first day of training, pellets were placed only in the largest well. When the total pellets retrieved on a given day exceeded 500, the next smaller well was used on the following day. Training was completed when the number of pellets retrieved from the smallest well exceeded 500 on 2 consecutive days. The Klüver board task was also used in the test session, when the daily changes in manual dexterity were evaluated. The test session consisted of 50 trials; in each trial, a pellet was placed pseudo randomly into a well such that 10 pellets were placed in each of the 5 differently sized wells over the course of the session. Manual dexterity was also evaluated by a task in which monkeys grasped and retrieved a small piece of food through a narrow vertical slit by using both the index finger and thumb. In this vertical slit task, the food piece ($7 \times 7 \times 7$ mm in size) was positioned in the center of a slit (30 mm in height and 10 mm in width) located at shoulder height and at a sagittal distance of

15 cm from the cage. This is a similar but slightly more difficult task than that used in our previous studies), which was performed with the monkey sitting in a monkey chair. Monkeys reached their hand out between the cage bars in the present vertical slit task, and thus a higher level of coordination between the hand and arm was required. The test sessions with the Klüver board task and vertical slit task were conducted before and after the training session, respectively. Food was restricted for 14–18 h before the test/training sessions with water available *ad libitum*. Supplemental feedings were given if adequate feeding was not obtained from the test/training sessions.

Wisconsin General Test Apparatus

According to the WGTA protocol,[66] monkeys were subjected to WGTA tests by trained technicians at the age of 1.5 years. The device includes a test box for observing the subject's activity, a display board with a food well for placing the reward, a test door connected by a pulley rope to separate the subject from the display board, and an access door. All tests were conducted in a quiet and standard-lit room.

MRI data acquisition

The brain of rhesus macaques was scanned regularly by a 3.0 T MRI machine (uMR 770, United Imaging Healthcare), and the changes in brain volume were analyzed at the same time. To prevent gastric regurgitation caused by the anesthetic, each animal was fasted for at least 6 h before MRI scanning. The animals in each group ($n = 3$) were scanned by MRI after anesthesia. Each animal was given ketamine hydrochloride solution (10 mg/kg, i.m.) and atropine sulfate injection (0.05 mg/kg, i.m.) before MRI scan to induce anesthesia and reduce bronchial and salivary secretions. Deep anesthesia was maintained with dexmedetomidine (0.05 mg/kg, i.m.). 3D T1-weighted images were acquired with these parameters: TR = 13 ms, TE = 5.6 ms, inversion time = 880 ms, FA = 8°, FOV = 96 mm × 80 mm, in-plane resolution of 192 μm × 100 μm, slice thickness = 500 μm. Resting-state functional MRI data were acquired with these parameters: TR = 1700 ms, TE = 29 ms, FA = 80°, FOV = 96 mm × 96 mm, in-plane resolution of 64 μm × 100 μm, slice thickness = 1500 μm.

Structural image processing

For structural image processing, we averaged all the T1 or T2 image of each subject using the 'AverageImages' function of software 'ANTs'[105] to get a finer image, then extracted the brain by the 'BEN' algorithm.[106] To obtain the cerebellar mask for each subject, we registered the reference NMT-V2's template to each subject's high age (e.g., 21m) T1 image and apply the transformation by the 'antsRegistrationSyN' and 'antsApplyTransforms' of ANTs, and then registered the cerebellar mask from high age to low age within the same individual. All cerebellar masks obtained were manually checked and corrected in the itksnaps[96] for further analysis. The cerebellar cortex were delineated into 17 regions on the template based on the paxinos atlas (including lingula I (I), central lobule II (II), culmen III (III), declive IV (IV), lobule V (V), folium VI (VI),tuber VII (VII), pyramid VIII (VIII), uvula IX (IX), nodulus X (X), simplex lobule (Sim), paramedian lobule (Par), copula (Cop), flocculus (Fl), PFL (PFl), Crus I, and Crus II).[71] The cerebellar cortex regions were also registered to each subject space with a similar but more precise 'cerebellum to cerebellum register' methods. The regions images were finally smoothed with 0.5 mm by the '3dLocalstat' method of AFNI[98] to remove artificial information.

Surface reconstruction and geometric analysis

The cerebellar outer contour surface were extracted by the cerebellar mask using the 'mri_tessellate' and 'mris_extract_main_component' methods of Freesurfer,[99] and the outer contour surface area was calculated using the wb_command -surface-vertex-areas method of Connectome Workbench.[97] For the analysis of the morphological, the first four geometric eigenmodes were generated by the cerebellar outer contour surface using the eigenmode decomposition.[107] We use the maximum value minus the minimum value for each geometric eigenmode to obtain the value used to represent the distance traveled by this geometric eigenmode, which represents the length of the change in the direction of this geometric eigenmode.

Functional MRI analysis

For the fMRI data, spike artifacts removing, slice-timing correction, head-motion correction were performed using 3dDespike, 3dTshift and 3dvolreg function of AFNI,[98] respectively. The preprocessed fMRI data were spatially registered to the T1 or T2 images of each subject by a rigid-body transformation and registered to the NMT-V2 template by an affine and a nonlinear transformation using the ''antsRegistrationSyN'' routine of ANTs. The registered fMRI cerebellar data of were mapped to a 3D surfaces of cerebellum and spatially smoothed with a 0.5 mm FWHM kernel on the cerebellar surface using the wb_command of Connectome Workbench. And the registered fMRI cerebral cortex data were spatially smoothed with a 1 mm FWHM kernel on the volume space using the 3dBlurInMask function of AFNI.

Analysis of survival rate and apoptosis

Primary fibroblasts from macaque skin were plated in 6-multiwell plates different densities and treated after 48 h with increasing doses of irradiation. After 5 days, cells were fixed and stained with crystal violet for cell counting. Apoptosis was identified by using FITC Annexin V Apoptosis Detection Kit I (BD). Fibroblasts were plated in 6-multiwell plates and treated after 48 h with the indicated treatments. After 12 h, cells were incubated as described by the manufacturers. Briefly, cells were rinsed three times in 1× PBS and

then incubated in 1× PBS supplemented with Annexin V-FITC and PI for 30 min at room temperature. FACS analysis for each sample was carried out on an LSR Fortessa flow cytometer (BD Biosciences). Up to 30,000 cells were analyzed for each condition, and data analysis was performed using FlowJo software.

Tissue collection

Following a 24-month postnatal observation, a pair of sex- and age-matched macaques were anesthetized, and subsequently, a saline solution was perfused systematically through heart. The tissues from different systems were then collected. Fresh tissues were sampled and stored in freezing tubes in liquid nitrogen. The remaining tissues were fixed with 4% paraformaldehyde, embedded in OTC (Leica) and cryopreserved in −80°C freezers.

Immunohistochemical and fluorescent staining

Animals were deeply anesthetized with dexmedetomidine (0.05 mg/kg, i.m.) and perfused with PBS (0.1 M). For immunohistochemical analysis, the brain tissue was sectioned in paraffin slicer (Leica, HistoCore BIOCUT) at a thickness of 10 microns. Immunohistochemical staining and hematoxylin-eosin (HE) staining were performed. Digital images taken using a slide scanner (Pannoramic, 250 Flash III). Immunohistochemical sections were washed three times with 0.01 M phosphate buffered saline (PBS, pH 7.4) and incubated with primary antibody at 4°C overnight. After incubation of the primary antibody, the corresponding secondary antibody incubated slices were left in the dark at room temperature for 3 h. Sections were covered with a lid containing DAPI (Abcam) and scanned under a fluorescence microscope (Leica TCS SP8). The staining results were analyzed using the ImageJ software.

Western blotting

Tissues were homogenized in RIPA buffer (containing 50 mM Tris-HCl, pH 7.4, 150 mM NaCl, 1% Triton X-100, 0.1% SDS, 1% sodium deoxycholate, protease inhibitor cocktail and phosphatase inhibitor cocktail) on ice and then centrifuged at 1,000 g for 10 min at 4°C. The supernatant was stored at −80°C until use. Protein concentration was measured with BCA method. Approximately 30 μg protein of each sample was loaded in on 10% SDS–PAGE and run at 120 V constant voltage. A constant current of 0.36 mA was used for transblotting. Blots were probed with primary antibodies overnight at 4°C. After washing three times, blots were then incubated with secondary antibody at room temperature for 2 h. Chemiluminescence was used to visualize protein bands.

In situ direct DNA fragmentation (TUNEL) assay

To measure damaged DNA in macaque cerebellum, a terminal deoxynucleotidyl transferase-mediated-dUTP nick-end labeling (TUNEL) staining was used following the manufacturers protocol. As a positive C1, brain slides were treated with DNase to induce DNA damage. Images were obtained by fluorescence microscopy.

Golgi stain

Tissue preparation and tissue staining were performed according to the manufacturer's instructions, using the FD Rapid GolgiStain kit (FD NeuroTechnologies, Inc.; PK401 Cell Systems Biology).[72] Briefly, the cerebellar samples are 1.5–2 mm thick and immersed into the dipping solution (solution of the same volume of A and B). After two weeks (first 24 h after solution change A/B), the tissue was transferred to solution C and stored at room temperature for 72 h (first 24 h after solution change C), parts were transferred to PBS and cut to 100 μm thickness using Vibratome (VT1200S; Leica). Imaging of Golgi-stained Purkinje neurons for Sholl analysis and dendritic analysis was performed using an Olympus FV1000 confocal microscopy system. Using ImageJ software, Sholl analysis was performed on each Purkinje neuron. Concentric rings each increased in radius by 10 μm were layered around the cell body until dendrites were completely encompassed. Dendrite length was measured within a concentric ring area and plotted. Branching points (nodes) were reported as the number per concentric ring area. Intersections were determined as the number of points where the processes crossed a concentric ring.

Transmission electron microscopy method

The samples were fixed overnight at 4°C using 2.5% glutaraldehyde in 0.1 M PBS (PH7.2), then washed with 0.1M PBS (PH7.2) three times for 7 min. Afterward, samples were postfixed with 1% OsO_4 for 2h at 4°C, then washed with ddH_2O three times for 7 min, followed by serial ethanol dehydration and acetone transition for 5min, embedding in SPI pon 812 resin, polymerization at 60°C for 48 h. Serial sections of uniform thickness, 60 nm for ultrathin sections, were made using a Leica EM UC7 ultramicrotome. Ultrathin sections were then loaded onto Cu grids and double stained with 2% uranyl acetate and lead citrate before observations employing a JEM-1400 Plus transmission electron microscope at 80 kv.

Nuclei isolation

The collected tissues were washed by 1× PBS, then quickly frozen and stored in liquid nitrogen. Nuclei extraction was separated by mechanical extraction method.[108] Firstly, put the tissues into a 2 mL Dounce homogenizer set and thawed in homogenization buffer (containing 20 mM Tris pH8.0, 500 mM sucrose, 0.1% NP-40, 0.2U/μL RNase inhibitor, 1× protease inhibitor cocktail, 1% bovine serum albumin (BSA), and 0.1 mM DTT. Use Dounce pestle A to grind the tissue 10 times, filter with 70 μm cell filter, and then grind with Dounce pestle B 10 times, filter with 30 μm cell filter. Centrifuge at 500 g for 5 min at 4°C to pellet the nuclei, and resuspend in the

blocking buffer containing 1% BSA and 0.2 U/μL RNase inhibitor in 1× PBS. Centrifuge again at 500 g for 5 min and resuspend with Cell Resuspension Buffer (MGI).

Single-nucleus RNA library construction and sequencing

DNBelab C Series High-throughput Single-Cell RNA Library (MGI) was utilized for snRNA-seq library preparation. In brief, the single-nucleus suspensions were converted to barcoded snRNA-seq libraries through steps including droplet encapsulation, emulsion breakage, mRNA captured beads collection, reverse transcription, cDNA amplification, and purification. cDNA production was sheared to short fragments with 250–400 bp, and indexed sequencing libraries were constructed according to the manufacturer's protocol. Qualification was performed using Qubit ssDNA Assay Kit (Thermo Fisher Scientific) and Agilent Bioanalyzer 2100. All libraries were further sequenced by the DNBSEQ-T7(MGI) sequencing platform with pair-end sequencing. The sequencing reads contained 30-bp read 1 (including the 10-bp cell barcode 1, 10-bp cell barcode 2, and 10-bp UMIs (UMI)), 100-bp read 2 for gene sequences and 10-bp barcodes read for sample index.

Single-cell sequencing data processing

We used the DNBC4tools, which is a Python package for DNBelab Series Single-Cell analysis workflow to process the sequencing reads of single-cell transcriptomics and align to rhesus macaque reference genome (Mmul_10), resulting in a preliminarily filtered gene-by-cell expression matrix. The output was processed using Seurat v4.3.0.1.[100] We then applied standard filtering (nGene $\geq$ 200, nUMI $\geq$ 200, nGene $\leq$ 5000, nUMI $\leq$ 25000, percent.mt $\leq$ 5) and removed doublets (Assuming 7.5% doublet formation rate) using doubletFinder_v3 function from DoubletFinder v2.0.3 (Figure S7B).[78] The quality C1 statistics are listed in Table S1 and the filtered violin plots are presented in Figure S1A. We used NormalizeData, FindVariableFeatures and ScaleData function of Seurat to normalize and scale the Seurat object with LogNormalize method. And we used harmony (v1.2.0)[102] to integrate the sample snRNA-seq data of ATM-deficient (A1) and healthy C1 cerebellums (The annotated integration results are shown in Figure 7B). We further quantified the proportion of A1 cells and C1 cells within each cell type (Figure 7D). Cell that passed the filtering and integrating were clustered and annotated based on manual curation using published markers from human and mouse cerebellum.[81,109]

Genes were differentially expressed between A1 and C1 were defined for each cluster using the FindMarkers function of Seurat. And we performed GO enrichment analysis based on DEGs using enrich GO function of clusterProfiler (v4.6.0) package.[41] To perform intercellular communication analysis, we transformed the macaque genes to human genes using gprofiler2 (v0.2.3).[80] CellChat (v1.6.1)[104] was used to analyze receptor-ligand interactions using standard processing and comparison analysis between A1 and C1 was performed based on human ligand-receptor interactions database.

QUANTIFICATION AND STATISTICAL ANALYSIS

For cellular and animal experiments, statistical parameters including statistical analysis and statistical significance reported in the figure legends and supplementary figure legends were determined by two-tailed Student's t test. GraphPad Prism 9 was used to perform the bar graphs or line graphs. MRI analyses and visualizations were performed in MATLAB version 2020a (MathWorks), ITK-SNAP Version 3.8.0, Connectome Workbench Version 1.4.2, AFNI Version 22.1.10, and Freesurfer Version 3.0. Bioinformatic quantitative and statistical analyses of snRNA-seq data were performed using the R and python computational environment and packages. More details can be found in the relevant sections of the method details.

ADDITIONAL RESOURCES

This study did not generate any additional resources.

Cell Reports Medicine, Volume *6*

Supplemental information

ATM deficiency drives phenotypic diversity and Purkinje cell degeneration in a macaque model of ataxia-telangiectasia

Kaiyu Xu, Ying Zhang, Yongxuan Chen, Xiaojia Zhu, Yu Li, Longbao Lv, Xiechao He, Zhengfei Hu, Yifan Li, Maosen Ye, Dewei Jiang, Zhanlong He, Weihua Jin, Yanyan Li, Xiaomei Yu, Deng-Feng Zhang, Karl Herrup, Ping Zheng, Yong-Gang Yao, Dong-Dong Wu, and Jiali Li

A

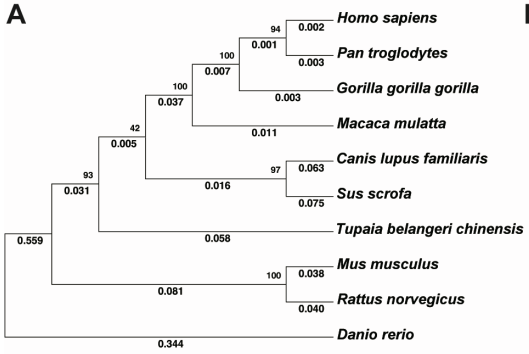

B

Component	Sequence	Target location	Concentration (ng/μL)
sgRNA1	UUGUUUCAGGAUCUCGAAUC	Exon 3 (anti-sense)	133
sgRNA2	CGGCAUUCAGAUUCCAAACA	Exon 3 (sense)	133
Cas9 protein	-	-	300

C

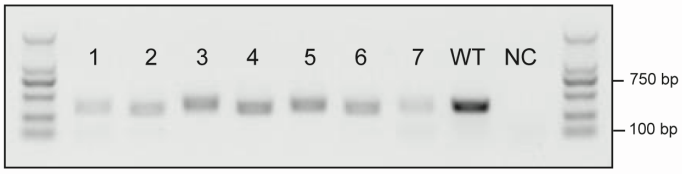

WT, wild-type; NC, negative control

E

Embryo	Stage	Genotype
1	16 cells	*ATM* $^{-/-}$
2	8 cells	*ATM* $^{-/-}$
3	8 cells	*ATM* $^{+/-}$
4	8 cells	*ATM* $^{-/-}$
5	broken	*ATM* $^{-/-}$
6	8 cells	*ATM* $^{-/-}$
7	4 cells	*ATM* $^{-/-}$

Tested on the third day after microinjection

D

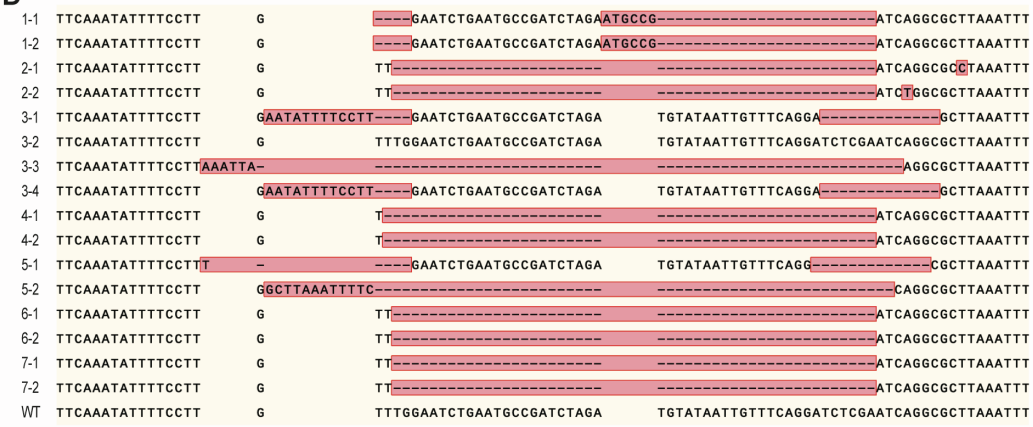

F

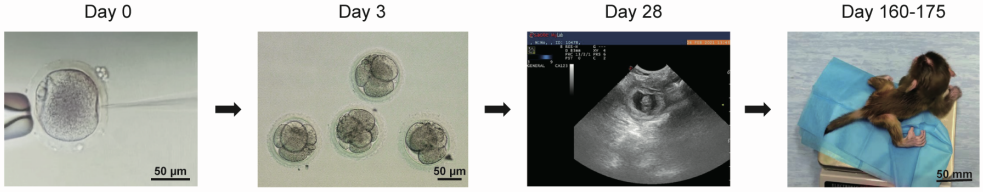

G

Oocytes	Injected embryos	Embryos of ET	Pregnancies/ surrogates	Miscarried fetus	Full-term fetuses	
					Live	Positive (%)
122	88	55	16.67% (3/18)	0	3	3 (100%)

H

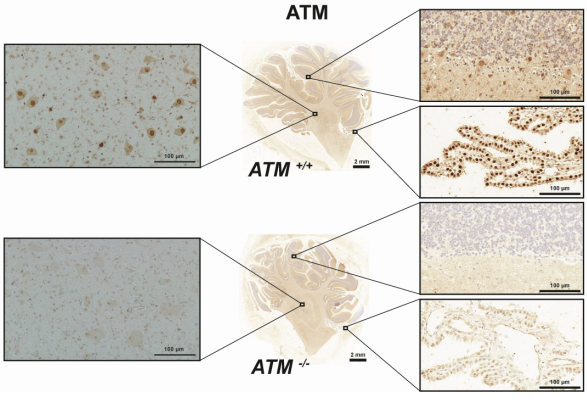

Figure S1. Generation of CRISPR/Cas9-mediated ATM-deficient macaques, related to Figure 1

(A) Conservation analysis of the ATM protein sequences showed the higher conservation ratio between macaque and human compared with that of mouse, indicating the higher conservation between primates. Data from UniProt: www.uniprot.org.

(B) Sequences and concentrations of the components used in the macaque embryo assay, including sgRNAs and Cas9 protein.

(C-D) Different types of mutations identified by PCR-amplified *ATM*-DNA from sgRNAs/Cas9-injected macaque embryos (C) and Sanger sequencing validation (D). WT, wild-type embryo; NC, negative control. (D) Alignment of partial *ATM* sequences genotyped from embryo DNA, showing the specific mutations introduced by the CRISPR/Cas9 editing.

(E) Editing efficiency of the embryos, indicating the proportion of successfully edited embryos.

(F) Schematic representation of the process used to generate ATM-deficient macaques via CRISPR/Cas9-mediated genome editing. Scale bars: 50 μm and 50 mm.

(G) Summary of embryo microinjection and transplant procedures, detailing the injection of RNPs into macaque embryos.

(H) Immunohistochemical staining for ATM in cerebellum sections from a control (C1; $ATM^{+/+}$) and an ATM-deficient macaque (A1; $ATM^{-/-}$). Scale bars: 2.0 mm (*mid*) and 100 μm (*left* & *right*).

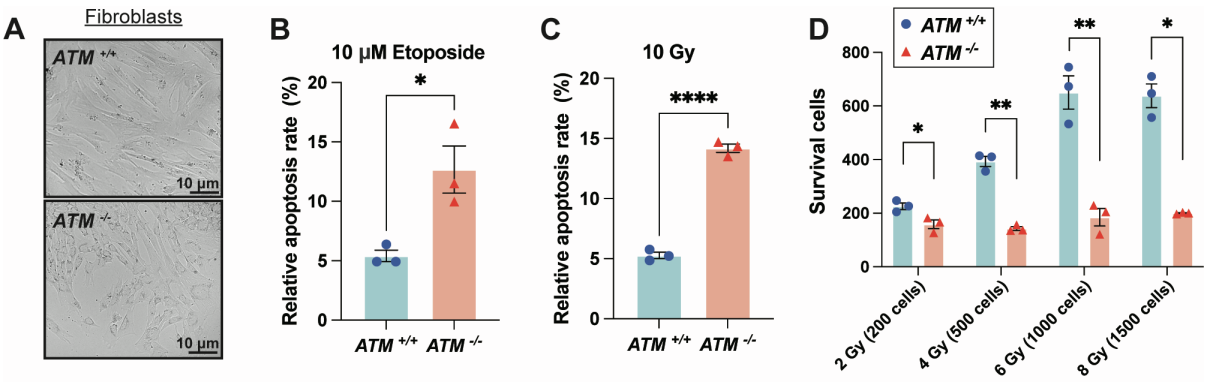

Figure S2. Phenotypes in multiple systems of ATM-deficient macaques, related to Figure 2

(A) Cultured primary fibroblasts from macaque ear skin. Scale bar, 10 μm.

(B-C) ATM-deficient fibroblasts show increased sensitivity to ionizing radiation and DNA damage. Relative apoptosis rates of fibroblasts treated with etoposide (B, assessed by Annexin V/PI assay) and irradiation (C).

(D) Cell survival after irradiation at different doses, with the initial cell number indicated in parentheses.

Data in (B-D) are presented as mean ± SEM, $n = 3$ macaques per group; ∗, $p < 0.05$; ∗∗, $p < 0.01$; ∗∗∗∗, $p < 0.0001$; unpaired t-test.

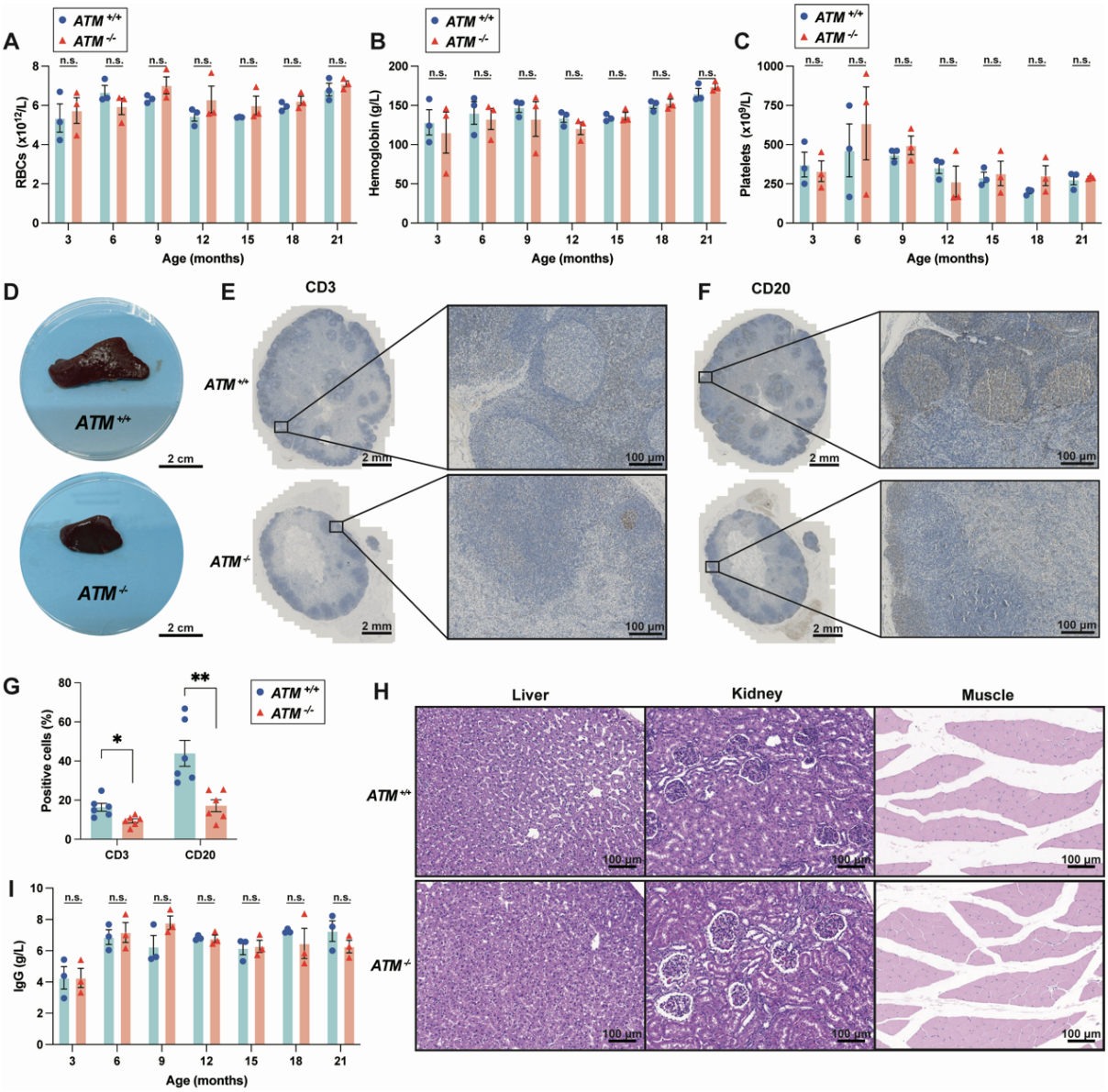

Figure S3. ATM-deficiency results in immune dysfunction in macaques, related to Figure 3

(A-C) Peripheral blood analysis of red blood cells (A), hemoglobin (B), and platelets (C) during development. Data are presented as mean ± SEM, with $n = 3$ macaques per group; n.s., no significance; unpaired t-test.

(D) Representative spleen images of control (C1; $ATM^{+/+}$) and ATM-deficient (A1; $ATM^{-/-}$) macaques at 24-months. Scale bar, 2 cm.

(E-G) Immunohistochemical staining for CD3 (E) and CD20 (F) in axillary lymph node sections from control (C1) and ATM-deficient (A1) macaques. CD3 marks T-lymphocytes, and CD20 marks B-lymphocytes. Scale bar: left panels, 2 mm; right panels, 100 μm. (G) Quantification of positive cells in (E) and (F). Data are presented as mean ± SEM from at least two sections, with counts from six different visual fields. *, $p < 0.05$; **, $p < 0.01$; unpaired t-test.

(H) Representative images of hematoxylin and eosin (HE) staining of liver, kidney, and muscle tissues from ATM-deficient (A1) and control (C1) macaques. Scale bar, 100 μm.

(I) Quantification of IgG levels in macaque serum. Data are presented as mean ± SEM, $n = 3$ macaques per group; n.s., no significance; unpaired t-test.

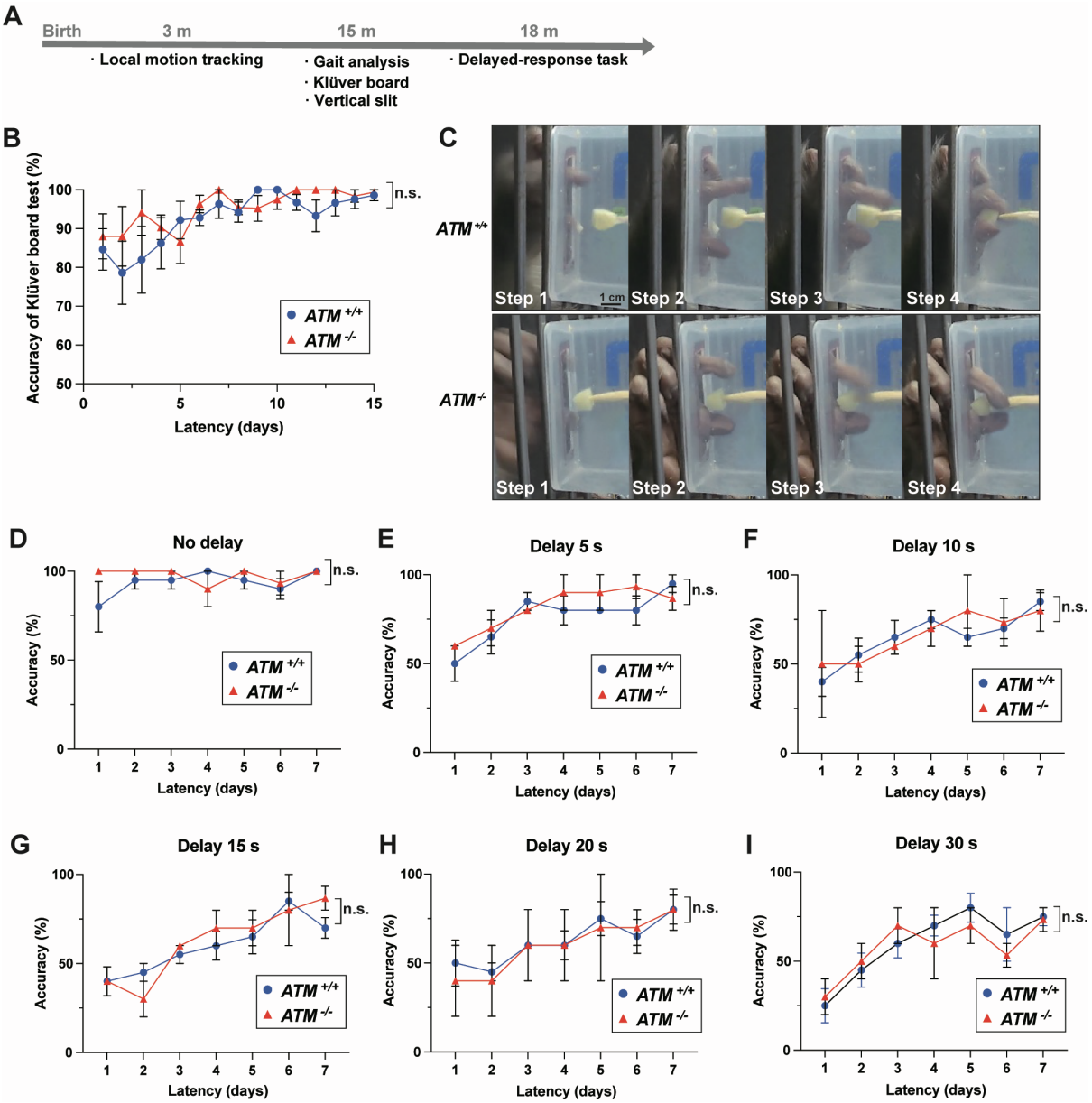

Figure S4. Behavior analysis of ATM-deficiency macaques, related to Figure 4

(A) Illustration of the workflow for behavioral experiments in all macaques.

(B) Accuracy of the Klüver board test. The X-axis represents the number of learning days, the Y-axis represents accuracy.

(C) Vertical slit test in macaques. The photographs show hand and digit movements of ATM-deficient (A1) and control (C1) macaques. Images sequentially depict (step 1) the moment of contact between the index fingertip and the slit, (step 2) the moment when the fingertips approach the food morsel, (step 3) contact of the thumb tip with the food morsel, and (step 4) digits withdrawing from the slit. Scale bar, 1 cm.

(D-I) Accuracy in location-matched memory tasks with varying delays: no delay (D), 5 s delay (E), 10 s delay (F), 15 s delay (G), 20 s delay (H), and 30 s delay (I). The X-axis represents the number of learning days, and the Y-axis represents accuracy.

Data in (B-I) are presented as mean ± SEM, n = 3 macaques per group; n.s., no significance; unpaired t-test.

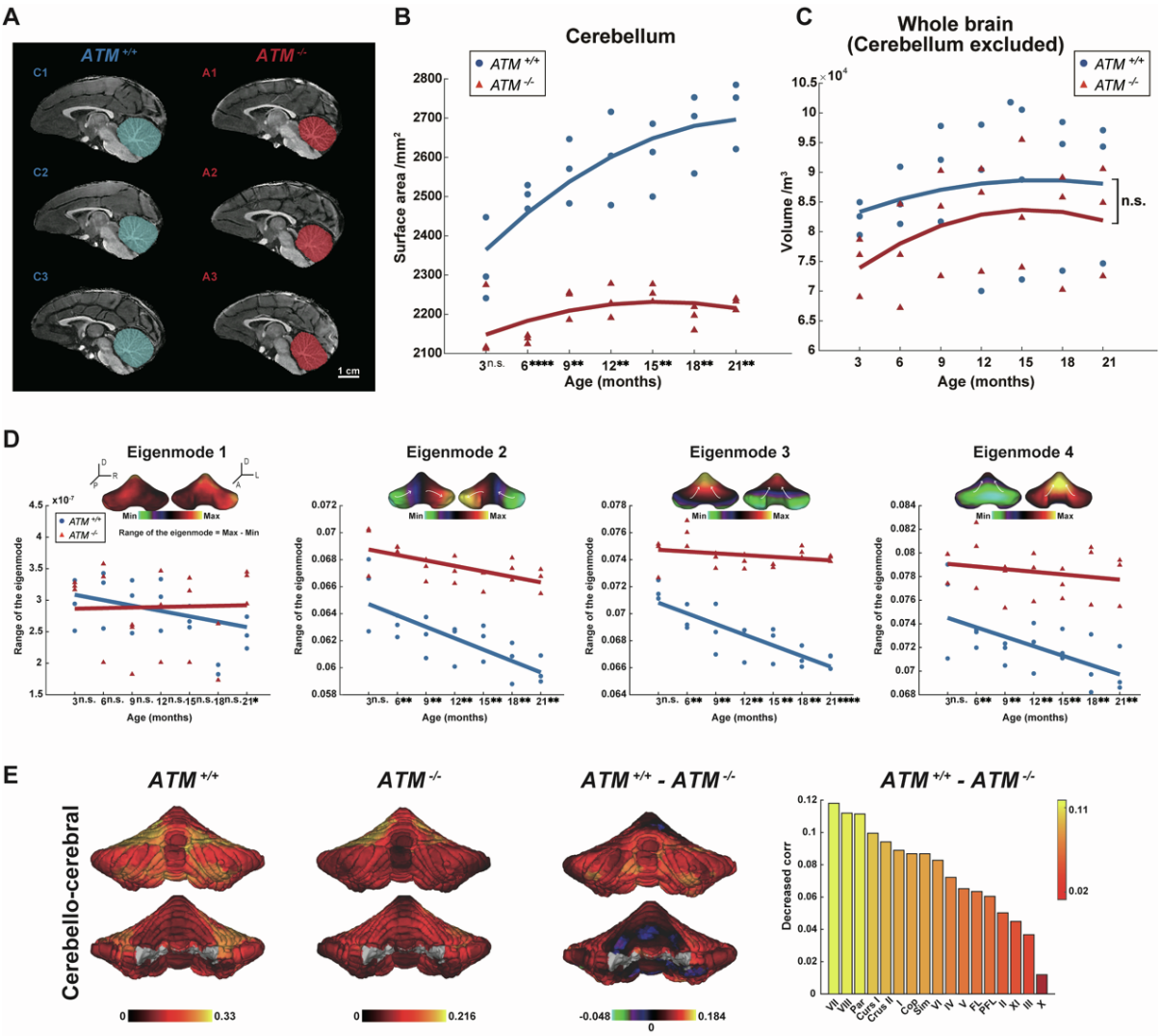

Figure S5. MRI analysis ATM-deficiency macaques, Related to Figure 5

(A) T1-weighted structural images of the cerebellum from 21-month-old control macaques (*left*) and ATM-deficient macaques (*right*). Scale bar, 1 cm.

(B) Surface area of the outer contour of the cerebellum in control ($ATM^{+/+}$; *blue*) and ATM-deficient macaques ($ATM^{-/-}$; *red*) over time. $n = 3$ per group, **, $p < 0.01$; ****, $p < 0.0001$; n.s., no significance; unpaired t-test.

(C) The brain volume excluding the cerebellum in control macaques ($ATM^{+/+}$, *blue*) and ATM-deficient macaques ($ATM^{-/-}$, *red*) at various time points. no significance; unpaired t-test.

(D) Differences in the first four geometric eigenmodes of the cerebellum between ATM-deficient and control groups. $n = 3$ per group; **, $p < 0.01$; ****, $p < 0.0001$; n.s., no significance; unpaired t-test.

(E) Average functional connectivity (FC) of cerebellar-to-cerebral pathways, with differences between ATM-deficient and control macaques.

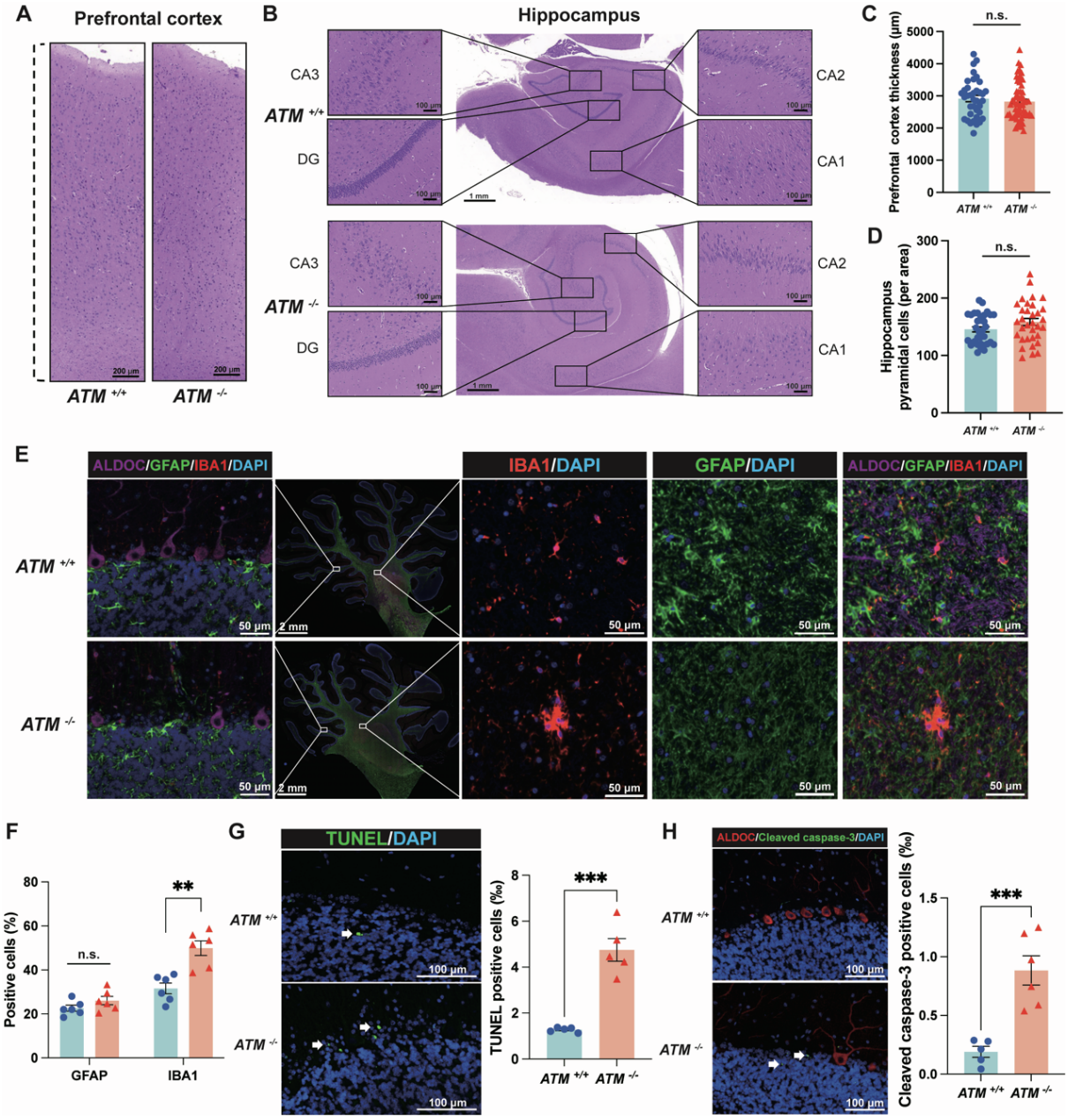

Figure S6. ATM-deficiency results in cerebellar-specific degeneration in macaques, related to Figure 6

(A-D) No major structural abnormalities were detected in the ATM-deficient cerebrum. Representative HE-stained sections of the prefrontal cortex (A) and the hippocampus (B) from an ATM-deficient (A1; *ATM*$^{-/-}$) and a control (C1; *ATM*$^{+/+}$) macaque. Scale bar: 200 μm in (A); 100 μm (flank panels) and 1 mm (center panel) in (B). (C-D) Quantification of prefrontal cortex thickness (C) and hippocampus cell numbers (D). Data are presented as mean ± SEM from at least two sections, with counts from ten different visual fields. n.s., no significance; unpaired t-test.

(E-F) Immunofluorescence staining of diverse cerebellar cells. (E) Representative immunofluorescence images for Purkinje cell (ALDOC; purple), astrocyte (GFAP; green), and microglia (IBA1; red). Scale bar: 50 μm (flank panels) and 2 mm (center panel). (F) Quantification of (E). Data are presented as mean ± SEM from at least two sections, with counts from six different visual fields. **, $p < 0.01$; n.s., no significance; unpaired t-test.

(G-H) DNA damage (G) and cellular apoptosis (H) were increased in ATM-deficient cerebellum (A1; *ATM*$^{-/-}$). (G) Representative images of TUNEL staining show green fluorescence (arrows) (*left*), indicating positive

TUNEL staining; nuclei are counterstained with DAPI (blue). Quantitative analysis of TUNEL-positive cells in cerebellar vermis (*right*). (H) Representative images of cleaved caspase-3 staining show green fluorescence (arrows) (*left*), indicating positive cleaved caspase-3 staining; Purkinje cells and nuclei are co-stained with aldolase C (ALDOC; red) and DAPI (blue), respectively. Quantitative analysis of cleaved caspase-3-positive cells in cerebellar vermis (*right*). Scale bar, 100 μm. Data are presented as mean ± SEM from at least two sections, with counts from at least five different visual fields. ∗∗∗, $p < 0.001$; unpaired t-test.

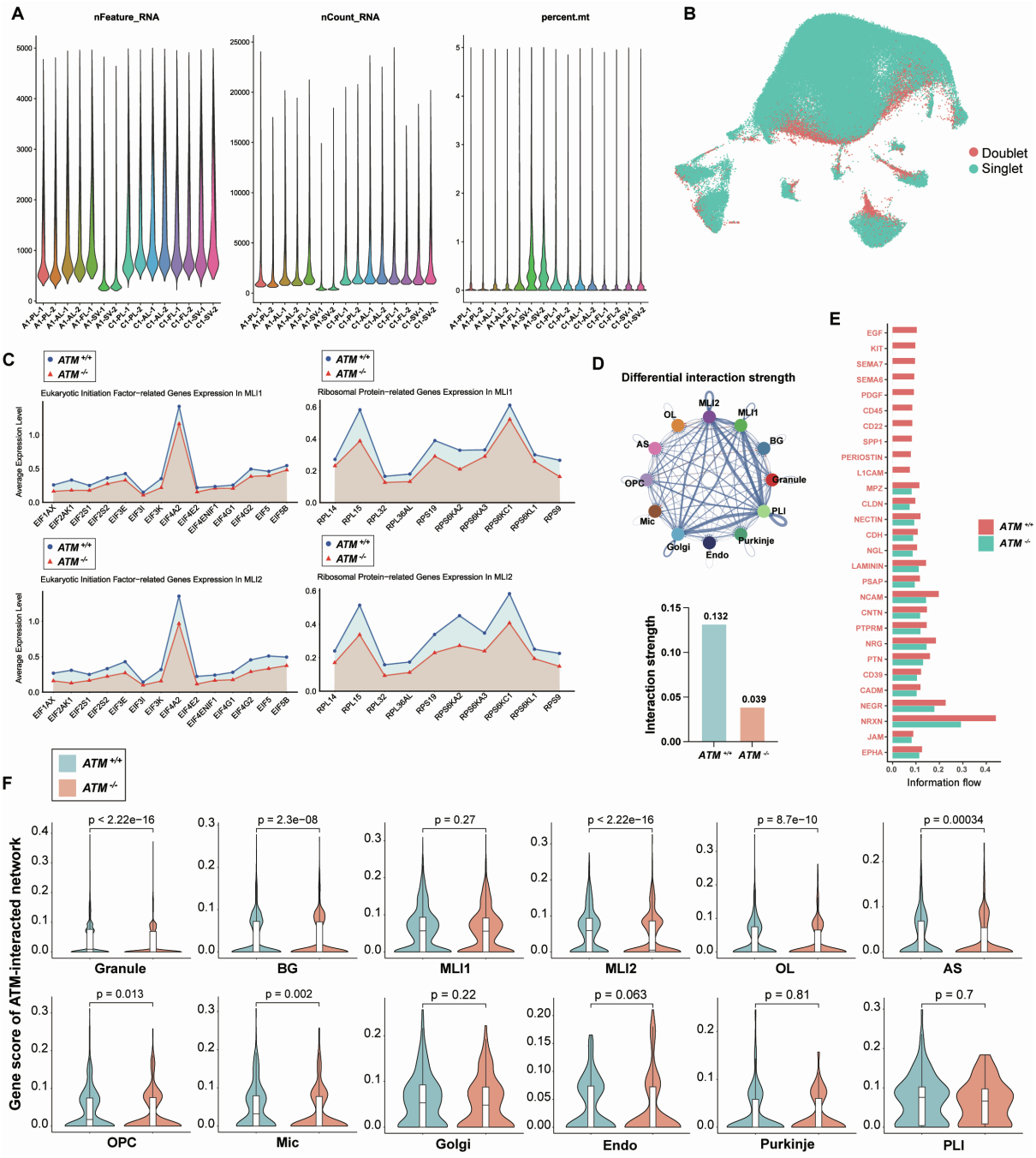

Figure S7. Single-cell transcriptomic atlas of neural cell types in the cerebellum of ATM-deficient macaque and control, related to Figure 7

(A) Violin plots displaying quality control metrics for single-cell transcriptome sequencing post-filtering. From left to right: the number of detected genes per cell, total RNA molecules per cell, and the percentage of mitochondrial gene expression. Each subregion has two technical replicates.

(B) Detection and filtering of doublets within the single-cell dataset.

(C) Expression levels of genes related to Eukaryotic Initiation Factor (EIF) and ribosomal protein functions in MLI1 (*top*) and MLI2 (*below*).

UMAP visualization showing the integration of single-cell datasets from ATM-deficient (A1; $ATM^{-/-}$) and control (C1; $ATM^{+/+}$) macaques.

(D) Overview of the intercellular communication networks in the interaction strength, the blue edge represents a

decrease in the interaction strength in A1 compared with C1 (*top*). Decrease interaction strength among the cells in A1 relative to C1 (*below*).

(E) Bar plots ranking signaling axes by overall information flow in the interaction networks of C1 and A1. The signaling pathways colored red are enriched in C1, and these colored green were enriched in A1.

(F) Gene score of 10 ATM-interacted genes in 12 types of cerebellar cells. Genes included in this analysis are: *MSH2*, *MSH6*, *NBN*, *TP53*, *MRE11*, *ATR*, *MDC1*, *TP53BP1*, *CHEK2*, *BRCA1*.

AS, astrocyte; Endo, endothelial cell; Mic, microglia; MLI, molecular layer interneuron; PLI, Purkinje layer interneuron; OL, oligodendrocyte; OPC, oligodendrocyte precursor cell; BG, Bergmann glia; Granule, granule neuron; Golgi, Golgi neuron; Purkinje, Purkinje cell.

Table S1. List of cerebellum regions sampled in this study.

Samples name	Macaque ID	Cerebellum regions	Number of cells in scRNA-seq dataset	Median UMI counts per cell	Median genes per cell
A1-PL-1	A1-21365	posterior lobe	8053	1064	634
A1-PL-2		posterior lobe	8912	947	582
A1-AL-1		anterior lobe	4943	1350	796
A1-AL-2		anterior lobe	6693	1173	712
A1-FL-2		Flocculus	3975	1484	815
A1-SV-1		Superior vermis	14278	434	307
A1-SV-2		Superior vermis	12516	457	323
W1-PL-1	C1-21367	posterior lobe	7567	1366	821
W1-PL-2		posterior lobe	8408	1482	910
W1-AL-1		anterior lobe	7542	1749	1011
W1-AL-2		anterior lobe	8611	1780	1035
W1-FL-1		Flocculus	6856	1565	893
W1-FL-2		Flocculus	10780	1456.5	873
W1-SV-1		Superior vermis	6612	1636.5	977
W1-SV-2		Superior vermis	6045	1886	1086

Cell counts for snRNA-seq are final counts after all quality control filters have been applied.

Table S2. The number of differentially expressed genes per cell type.

Cell type	Up-regulation of A1	Down-regulation of A1
Granule	1605	2126
BG	1342	1702
MLI1	922	3209
MLI2	2282	3078
OL	1556	1798
AS	1021	2501
Endo	63	888
Golgi	259	1973
Mic	714	2265
OPC	131	1131
Purkinje	85	814
PLI	139	689

AS, astrocyte; Endo, endothelial cell; Mic, microglia; MLI, molecular layer interneuron; PLI, Purkinje layer interneuron; OL, oligodendrocyte; OPC, oligodendrocyte precursor cell; BG, Bergmann glia; Granule, granule neuron; Golgi, Golgi neuron; Purkinje, Purkinje cell.